

**Analysis of performance degradation during steady-state and load-thermal cycles of proton exchange membrane water electrolysis cells**

Stefania Siracusano\*, Stefano Trocino, Nicola Briguglio, Fabiola Pantò, Antonino S. Aricò

CNR-ITAE Institute of Advanced Energy Technologies, National Research Council

Via Salita S. Lucia sopra Contesse 5, 98126 Messina, Italy

\*Corresponding author. Tel.: +39 090 624241; fax: +39 090 624247. E-mail address:

siracusano@itaecnr.it

**Abstract**

A membrane-electrode assembly based on a 90  $\mu\text{m}$  short-side-chain Aquivion<sup>®</sup> proton exchange membrane and containing low catalyst loadings, 0.4 mg IrRuOx  $\text{cm}^{-2}$  and 0.1 mg Pt  $\text{cm}^{-2}$  at anode and cathode, respectively, is investigated for combined thermal and load cycling at high current density (3 A  $\text{cm}^{-2}$ ) in water electrolysis cell. Durability tests under steady-state and load-thermal cycles are compared to evaluate the efficiency losses under specific operating conditions. Ac impedance spectra and post-operation analyses are carried out to investigate the degradation mechanism. Catalyst degradation occurs more rapidly under cycled operation whereas mass transfer issues are relevant especially under steady-state mode. Membrane thinning appears to be affected by the uptime hours at high current density. The overall cell voltage increase is slightly larger for the cycled operation compared to the steady-state mode. However, this is essentially related to a compensation effect associated to a larger decrease of series resistance during the steady-state durability test. The dynamic electrolysis mode at high current density does not exacerbate significantly the degradation issues of low catalyst loading MEAs compared to a steady-state operation. This confirms the proper dynamic characteristics of the polymer electrolyte membrane electrolyser.

**Keywords:** Electrolysis; Polymer electrolyte membrane; Hydrogen; Durability Steady-state tests; Load-thermal cycles.

## 1. Introduction

Electricity production from renewable sources can allow to reduce significantly CO<sub>2</sub> emissions and thus mitigate the effects of climate changes. The expected wide-scale diffusion of renewable energy sources will significantly contribute to the implementation of the new energy and environmental policy objectives to achieve the Paris CO21 conference targets.[1] Most of the future production of electricity is thus expected to come from renewable energy sources. However, because of the intermittent and unpredictable nature of renewable power production, an advanced energy storage is necessary to provide a proper solution for an efficient use of renewable sources such as solar plants and wind mills. [2-5] In the future, a large utilization of renewable power is expected to cause increasing energy management issues. This requires developing rapid-response, cheap and large scale energy storage systems capable of absorbing the surplus of electrical power. A large-scale energy storage will avoid relevant investments to develop a new grid infrastructure.

The excess of electricity, that cannot be transferred to the grid when there is no much request, can be utilized to produce high purity hydrogen by water electrolysis. This will allow efficient energy storage into a chemical compound acting as energy vector. Electrolysis can assist grid-balancing thus improving power quality, frequency and voltage control. In this regard, electrolysers should be designed to handle frequent start-stop cycles, dynamic operations and allow partial load operation. Specifically, electrolysers should be capable to handle variable energy input from renewable power sources locally available and have to adapt properly to the intermittent profile of electricity supply.

1  
2  
3  
4  
5  
6  
7  
8  
9  
10  
11  
12  
13  
14  
15  
16  
17  
18  
19  
20  
21  
22  
23  
24  
25  
26  
27  
28  
29  
30  
31  
32  
33  
34  
35  
36  
37  
38  
39  
40  
41  
42  
43  
44  
45  
46  
47  
48  
49  
50  
51  
52  
53  
54  
55  
56  
57  
58  
59  
60  
61  
62  
63  
64  
65

There are different technologies for water electrolysis: liquid alkaline electrolyte, polymer electrolyte membrane (PEM) and solid oxide electrolysers (SOECs). PEM electrolysers appear to be characterized by an appropriate dynamic behaviour and good flexibility for interfacing to renewable sources. [6-20]

In particular, proton exchange membrane water electrolysis possess the ability to rapidly follow the intermittent energy production from renewable power sources and can provide proper grid-balancing service to mitigate the differences in energy generation and consumption.

Sun et al. [21] reported a Proton Exchange Membrane Water Electrolysis (PEMWE) stack tested for 7800 h with an average degradation rate of  $35 \mu\text{V h}^{-1}$  per cell. They showed that the performance degradation of the stack was mainly caused by recoverable contaminations.

Frensch et al. [22] compared the performance over time of seven different operation modes (constant current, constant voltage, current cycling, etc.) to investigate the realistic degradation responses of a PEM WE for grid balancing services. They showed different advantages and disadvantages of different operation modes in terms of performance variation over time.

Rakousky et al. [23] investigated a PEMWE single cell for 1000 h observing a significant degradation rate of  $194 \mu\text{V h}^{-1}$ . They concluded that the 78 % of the detectable degradation can be explained by an increase in ohmic resistance.

Rakousky et al. [24] analysed the impact on investment costs of a PEMWE operating at elevated constant and intermittent current densities. They indicated that the PEMWE can be effectively coupled to intermittent power profiles from renewable energy sources without substantially affecting long-term stability.

In our previous works [25, 26], we have investigated the steady-state durability of PEM electrolysis cells containing different catalyst loadings. We have observed that the degradation rate is affected by the anode catalyst turn-over frequency operation. The degradation rate

1  
2  
3  
4  
5  
6  
7  
8  
9  
10  
11  
12  
13  
14  
15  
16  
17  
18  
19  
20  
21  
22  
23  
24  
25  
26  
27  
28  
29  
30  
31  
32  
33  
34  
35  
36  
37  
38  
39  
40  
41  
42  
43  
44  
45  
46  
47  
48  
49  
50  
51  
52  
53  
54  
55  
56  
57  
58  
59  
60  
61  
62  
63  
64  
65

increased in the presence of high operating current densities and especially for low anode catalyst loadings.

In this work, the dynamic behaviour of a PEM electrolysis cell containing low catalyst loadings was studied in order to understand its effect on performance degradation. The cell was based on well characterized materials such as a short-side chain Aquivion membrane [26-32] and a solid solution Ir and Ru oxide catalyst at the anode ( $0.34 \text{ mg cm}^{-2} \text{ Ir+Ru}$ ) [29, 33-35]. Two different operating conditions have been investigated using equivalent electrolysis cells. The first was operated in a steady-state condition at high current density ( $3 \text{ A cm}^{-2}$ ) whereas the second was subjected to load and thermal cycles. The degradation of the membrane-electrode assembly was studied by physico-chemical and morphological analyses.

## 2. Experimental

### 2.1 MEAs preparation

$\text{Ir}_{0.7}\text{Ru}_{0.3}\text{Ox}$  was used as anodic catalyst. It was synthesized by a modified Adams method [25, 29, 33]. Dry salts of metal precursors ( $\text{IrCl}_4 \cdot x\text{H}_2\text{O}$  and  $\text{RuCl}_3 \cdot x\text{H}_2\text{O}$ , Stream Chemicals) and  $\text{NaNO}_3$  (Aldrich) were treated in a furnace at  $500 \text{ }^\circ\text{C}$  for 3 min. The fused salt-oxide product was cooled down, washed, filtered and dried overnight in an oven at  $80 \text{ }^\circ\text{C}$ . To completely remove the sodium impurities, pre-leaching in  $\text{HClO}_4$  ( $0.1 \text{ M}$ ,  $80 \text{ }^\circ\text{C}$ , 15 min) was carried out. This procedure provided a crystalline nanosized IrRu-oxide (Ir:Ru = 70:30 at.%). A 40% Pt/C, prepared as described in ref. [36], was used as  $\text{H}_2$  evolution catalyst. A commercially available extruded short-side chain Solvay Aquivion<sup>®</sup> membrane (E98-09S) with an equivalent weight (EW) of  $980 \text{ g eq}^{-1}$  and a thickness of  $90 \text{ }\mu\text{m}$  was used as polymer electrolyte membrane separator. A catalyst-coated membrane (CCM) methodology was used for the preparation of MEAs [25]. The catalyst ink, composed of a dispersion of  $\text{Ir}_{0.7}\text{Ru}_{0.3}\text{Ox}$  and Aquivion<sup>®</sup> ionomer (D98-06AS) was directly spray-coated onto the

1 membrane. The cathode ink, consisting in a dispersion of Aquivion® ionomer and Pt/C, was coated  
2 onto the other membrane side. The ionomer contents in the electrodes were 15% and 28%  
3 wt. for the anode and cathode, respectively. The precious metal catalyst loadings were 0.34 mg  
4 IrRu cm<sup>-2</sup> (corresponding to 0.4 mg cm<sup>-2</sup> IrRu-oxide catalyst loading) and 0.1 mg Pt cm<sup>-2</sup> at anode  
5 and cathode, respectively. The formed CCMs (5 cm<sup>2</sup> geometric electrode area) were hot-pressed  
6 at 190°C, 1.5 min, 20 kg cm<sup>-2</sup>. A titanium fibre mesh (Bekaert Toko Metal Fiber Co.) was used as  
7 backing layer for the anode side. A carbon paper-based diffusion layer backing (GDL 39BB  
8 SIGRACET®) was used for the cathode side. The CCMs and the GDLs were assembled in an in-  
9 house designed titanium single cell test fixture (5 cm<sup>2</sup> geometric area). Deionized water, milli-Q  
10 Integral, Millipore was fed to the anode compartment with a flow rate of 1 mL min<sup>-1</sup>cm<sup>-2</sup> and  
11 recirculated at the same temperature of the cell. The water resistivity measured at the cell inlet  
12 was 18.18 MΩ. Before carrying out the initial polarisation measurements, a pre-conditioning  
13 procedure at 0.05 A cm<sup>-2</sup> for 24 h was carried out for each MEA to favour membrane and catalyst  
14 layers hydration and stabilisation of catalysts' oxidation state. Two equivalent MEAs were  
15 subjected to different durability tests under steady-state (1000 h) or mixed dynamic conditions  
16 (740 h).

## 2.2 Electrochemical characterization

23 The electrochemical measurements were performed at 80°C. Polarisation experiments were  
24 carried out by using a computer-controlled power supply module (TDK GEN 25-400-MD-3P400).  
25 Polarization curves were recorded in the galvanostatic mode by registering the cell voltage vs. the  
26 imposed current. At least three sets of polarisation curves were carried out under each condition  
27 to confirm data reproducibility (two in ascending mode, i.e., from the open circuit voltage to the  
28 highest current, and one in descending mode, i.e. from the highest current to the open circuit  
29

1 voltage). Electrochemical impedance spectroscopy (EIS) was performed with an Autolab PGSTAT-  
2 30 potentiostat/galvanostat (Metrohm) equipped with a 20 A current booster and FRA (frequency  
3 response analyser). Electrochemical impedance analysis was carried out in the potentiostatic  
4 mode at 1.5 V and 1.8 V. The frequency was varied from 100 kHz to 100 mHz (10 points per  
5 decade) in the single sine mode with a sinusoidal excitation signal of 10 mV rms. The steady-state  
6 test was recorded in galvanostatic mode at 1 A cm<sup>-2</sup> for 200 h and 3 A cm<sup>-2</sup> for 800 h 1000 h in  
7 total) with a cell cut-off voltage of 2.1 V (Fig. S1, supplementary material).

18 Specific protocols were used in order to test the MEA response under harsh conditions with  
19 high and low frequency load variation and under thermal cycles (Figs. S2, S3). For the load cycles  
20 at 80 °C, MEA conditioning steps of 24 h at 1 A cm<sup>-2</sup> and 100 h at 3 A cm<sup>-2</sup> were carried out before  
21 starting the current density (load) cycling test (Fig. S2). After the two initial steady-state steps, the  
22 cell was subjected to a first cycling procedure i.e. 9000, load cycles, consisting of 10 s at 0.2 A cm<sup>-2</sup>  
23 (~ 6% of nominal load) and 10 s at 3 A cm<sup>-2</sup> (partial - nominal load operating) for a total duration of  
24 50 h (Fig. S2). A steady-state operation of 50 h at 3 A cm<sup>-2</sup> preceded the second cycling procedure  
25 i. e. 9000 on-off cycles of 10 s at 0 A cm<sup>-2</sup> and 10 s at 3 A cm<sup>-2</sup> for 50 h (warm-start simulation).  
26 Another steady-state test of 50 h at 3 A cm<sup>-2</sup> preceded the third cycling procedure. This regarded  
27 45000, on-off cycles at high frequency, i.e. 2 s at 0 A cm<sup>-2</sup> and 2 s at 3 A cm<sup>-2</sup> for 50 h (Fig. S2). The  
28 fourth cycling step, on-off cycles at low frequency, was equivalent to the previous one but the cell  
29 was kept for 30 min at 0 A cm<sup>-2</sup> and at 3 A cm<sup>-2</sup> for 50 h with 50 cycles in total (low frequency  
30 cycling). The load cycling test ended with a 50 h steady-state at 3 A cm<sup>-2</sup> (Fig. S2). The duration of  
31 the specific load cycling test was 530 h (Fig. S2).

54 This dynamic test protocol was designed to i) carry a load cycling in a wide load range, i.e.  
55 from 0.2 to 3 A cm<sup>-2</sup> (from about 6% to 100% load), at an intermediate frequency (0.1 Hz), ii)  
56 evaluate warm-start up (from zero current to 3 A cm<sup>-2</sup> with pumps on and nominal temperature  
57  
58  
59  
60  
61  
62  
63  
64  
65

1 on) at intermediate frequency, iii) assess warm-start up at relatively high frequency (0.5 Hz), iv)  
2 assess warm-start up at relatively low frequency ( $\sim 5 \cdot 10^{-4}$  Hz). The high frequency step was dealing  
3 with a specific grid balancing service condition (grid stabilization against spikes). These  
4 characteristics for the electrolyser dynamic behaviour assessment were derived after an analysis  
5 of the power fluctuations associated to wind mills operation in winter in north-Europe (EU H2020  
6 FCH JU, HPEM2GAS project). [37]  
7  
8  
9  
10  
11  
12  
13  
14

15 In a subsequent test, the same cell was subjected to both load and thermal cycles (220 h) to  
16 simulate a cold start-up (Fig. S3). Seven steady-state steps including different temperatures and  
17 current densities were applied. The first steady-state step was for 24 h at  $0 \text{ A cm}^{-2}$  and  $25 \text{ }^\circ\text{C}$ ,  
18 followed by 24 h at  $3 \text{ A cm}^{-2}$  and  $80 \text{ }^\circ\text{C}$ , and thereafter a steady-state of 72 h at  $1 \text{ A cm}^{-2}$  and  $25 \text{ }^\circ\text{C}$ .  
19  
20  
21  
22  
23  
24  
25  
26  
27  
28  
29  
30  
31  
32  
33  
34  
35  
36  
37  
38  
39  
40  
41  
42  
43  
44  
45  
46  
47  
48  
49  
50  
51  
52  
53  
54  
55  
56  
57  
58  
59  
60  
61  
62  
63  
64  
65

A cold start procedure was assessed in this steady-state test, combining load and thermal cycles protocol (Fig. S3) passing from the first to the second step. In the third step, a partial load operation at low temperature was simulated. The next steps have regarded cold start-up cycles. The cycling procedure, carried out in the last 210 h, has dealt with tertiary reserve energy storage.

The two protocols reported in figs S2 and S3, load cycles of 530 h and combined thermal-load cycles 210 h (dynamic operation), were applied in sequence to evaluate the effects of steady-state operation, load cycles and thermal cycles in order to simulate practical operation of an electrolysis system in grid-balancing applications. The overall dynamic test was thus lasting about 740 h. As discussed earlier, an equivalent cell was subjected to a simple steady-state operation at  $1 \text{ A cm}^{-2}$  for 200 h and  $3 \text{ A cm}^{-2}$  for 800 h (Fig. S1) to compare degradation under dynamic and steady-state operation.

### 2.3 Morphologic and surface analyses

1 Morphological and surface characterizations were carried out on both fresh and used MEAs.  
2 Scanning Electron Microscopy (SEM) with Energy Dispersive X-Ray (EDX) analysis was carried out  
3  
4 by a FEI XL30 SFEG microscope. The instrument was operated at 25 kV and the EDX probe was  
5  
6 used to determine the bulk elemental composition of the anode electrodes before and after the  
7  
8 durability tests.  
9  
10

11  
12 The morphology of the IrRuOx and Pt/C electrodes was investigated by transmission electron  
13  
14 microscopy (TEM) using a FEI CM12 instrument. The specimens were prepared by ultrasonic  
15  
16 dispersion of the electrode in isopropyl alcohol and subsequently depositing a drop of the  
17  
18 suspension on a carbon-coated copper grid. The surface composition of the IrRu oxide-based  
19  
20 anodes, before and after durability tests including the overall dynamic test consisting of both  
21  
22 load and thermal cycle tests, was investigated by using a Physical Electronics (PHI) 5800-01 X-  
23  
24 ray photoelectron spectrometer (XPS).  
25  
26  
27  
28  
29

30 A monochromatic Al K $\alpha$  X-ray source was used at a power of 300 W. Spectra were  
31  
32 obtained with a pass energy of 58.7 eV for elemental analysis (composition) and 11.75 eV for the  
33  
34 determination of the chemical species. The pressure in the analysis chamber of the spectrometer  
35  
36 was  $1 \times 10^{-9}$  Torr during the measurements. Spectra were collected at a photo-electron take-off  
37  
38 angle of  $45^\circ$  with respect to the sample surface.  
39  
40  
41  
42  
43  
44  
45

### 46 **3. Results and discussion**

#### 47 **3.1 Electrochemical characterization**

48  
49 A polarization curve at 80 °C and ambient pressure of the fresh PEM electrolysis MEA based on an  
50  
51 Ir<sub>0.7</sub>Ru<sub>0.3</sub>Ox anode and a 40% Pt/C cathode electrocatalysts and extruded Aquivion® membrane  
52  
53 (E98 09S) is shown in Fig. 1. The overall precious metal catalyst loading was  $0.44 \text{ mg cm}^{-2}_{\text{MEA}}$  (Fig.  
54  
55 1a). The range of current density here investigated varied between 0 to  $4 \text{ A cm}^{-2}$ . Different sets of  
56  
57  
58  
59  
60  
61  
62  
63  
64  
65



polarisation curves were carried out to confirm data reproducibility. A comparison of polarisation curves, both in ascending mode, as well as polarisation curves carried out in ascending and descending modes are shown in Fig. S4a-b. No significant deviation or curve hysteresis was observed (standard deviation was < 5 mV for each data-point of the overall polarization data-set).

At 80 °C, a current density of 3 A cm<sup>-2</sup> was obtained at 1.82 V with a voltage efficiency of 81 % with respect to the high heating value (HHV) of H<sub>2</sub>. Operation at high current density allows a significant reduction in capital costs of the PEM electrolysis system [25, 26]. However, being the price of green hydrogen also affected by the cost of renewable energy, operation at high voltage efficiency is also particularly relevant. A nominal load of 3 A cm<sup>-2</sup> represents a good trade-off for these MEAs [25].

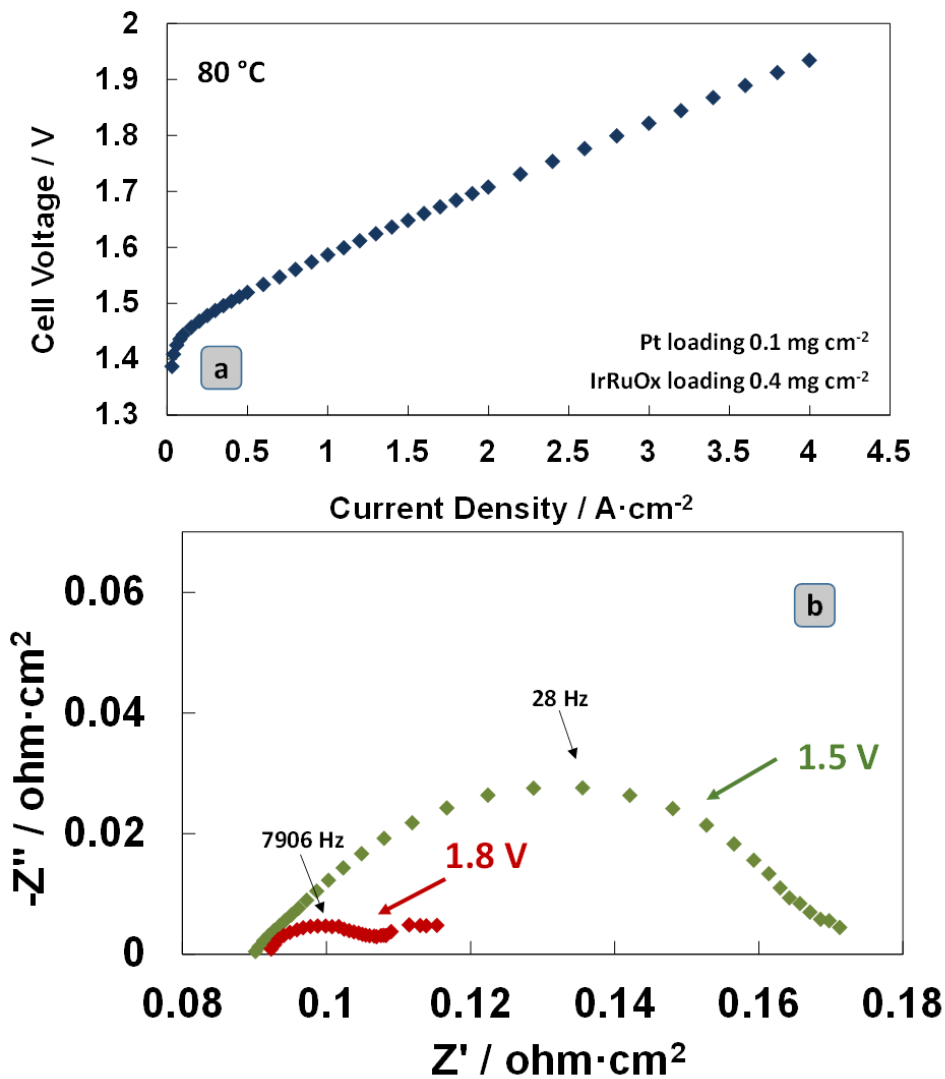


**Fig. 1** (a) Polarization curves at 80 °C and (b) ac-impedance spectra at 1.5 V and 1.8 V for the fresh PEM electrolysis MEA.

Electrochemical impedance analysis was carried out under two constant cell voltage conditions, i.e., 1.5 V and 1.8 V, and reported in terms of Nyquist plots in Fig. 1b. The ac-impedance spectra in the low voltage region (1.5 V) show a series resistance (high frequency intercept on the real axis) of 90 mOhm cm<sup>2</sup> and a polarisation resistance (difference between low and high frequency intercepts) of 81 mOhm cm<sup>2</sup> at 80 °C. At high cell voltage (1.8 V), a similar series resistance was recorded (92 mOhm cm<sup>2</sup>), whereas a lower polarization resistance, of 23

mOhm  $\text{cm}^2$  was observed. The series resistance is mainly associated to the membrane contribution and it dominates the overall polarization behaviour at high cell voltages. In particular, the role of the membrane is significant (>75% contribution) at a high current density of  $3 \text{ A cm}^{-2}$ . Assuming an optimal electronic percolation in the catalyst layers and current collectors, this means that at high currents the differential resistance in the polarisation curves is mainly determined by the membrane resistance.

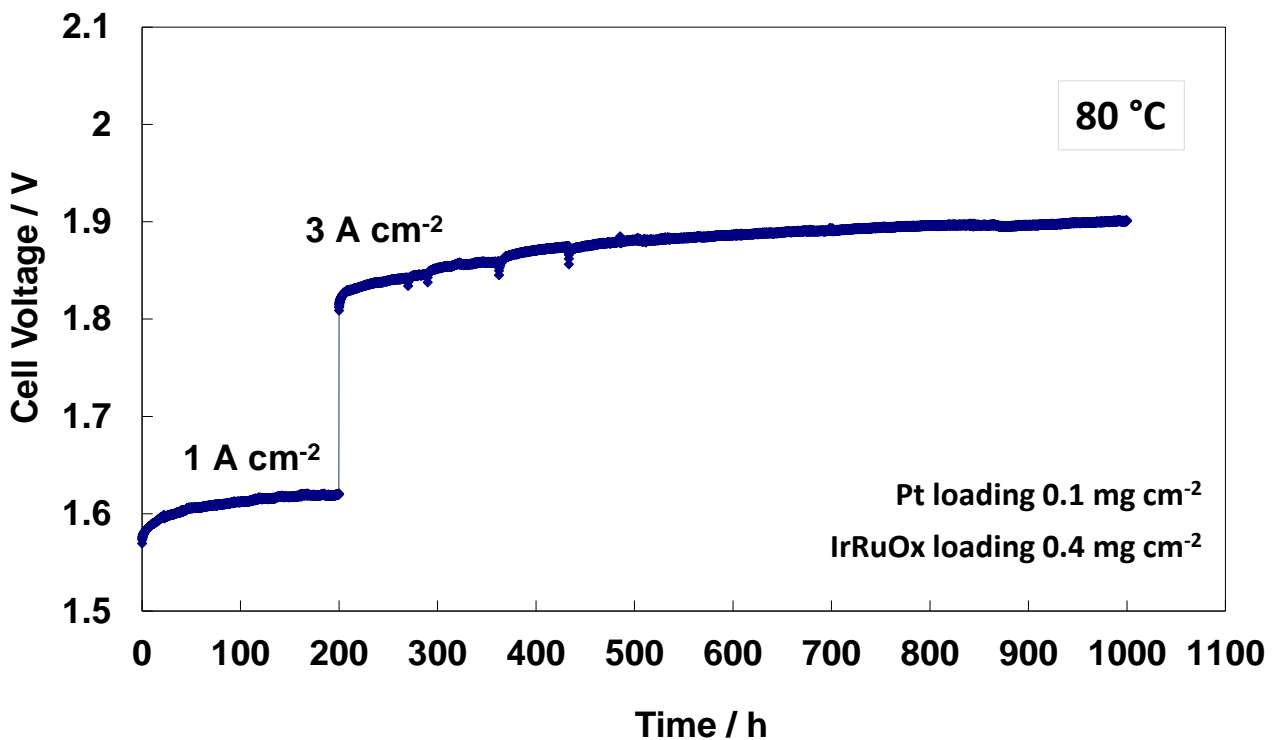


**Fig. 2** MEA steady-state durability test at 1 and  $3 \text{ A cm}^{-2}$  and  $80 \text{ }^\circ\text{C}$

A steady-state durability test was initially carried out at  $1 \text{ A cm}^{-2}$  for 200 h; thereafter, the current was switched at  $3 \text{ A cm}^{-2}$  for 800 h (Fig. 2). The overall steady-state test was thus lasting 1000 h. The first 200 h at low current density were appropriate for conditioning the electrolysis cell.

A sudden increase of the cell voltage was initially observed after the initial current switch. Similarly, a rapid increase of voltage with time was evident after the cell switch at higher current density ( $3 \text{ A cm}^{-2}$ ). In general, stabilisation of cell voltage does not occur immediately when a

1 significant increase of the operating current density is operated [26, 38]. This could be possibly  
2 ascribed to two main phenomena occurring under electrolysis conditions i.e. a mass transfer  
3 polarisation or a modification of the oxidation state at the anode surface according to the  
4 operating potential window (see below).  
5  
6  
7  
8  
9

10 The performance decay that has been registered in the overall test at 3  $\text{A cm}^{-2}$  was about 90  
11  $\mu\text{V/h}$  (considering the overall time window). However, the degradation rate reduced progressively  
12 to 33  $\mu\text{V/h}$  in the last 300 h of operation at 3  $\text{A cm}^{-2}$ . As observed, the increase of cell voltage  
13 appears to be affected, to some extent, by recoverable losses. These are in part recovered by  
14 decreasing to zero the operating current (rest interval).  
15  
16  
17  
18  
19  
20  
21  
22

23 The occurrence of reversible losses possibly associated to mass transport issues have been  
24 discussed in the literature [39]. In the PEM electrolysis case, mass transfer issues are not much  
25 related to the provision of water at the interface being the ionomer in the catalyst layer highly  
26 hydrophilic but to the accumulation of the evolved gases in the catalyst micropores forming a  
27 diffusion barrier for the produced gas to escape from the catalytic layer. In other words,  
28 recoverable losses may be possibly related to an entrapping effect of the evolved gases in the  
29 catalyst micropores and to the gas supersaturation in the catalytic layers [39]. In fact, the  
30 occurrence of such supersaturation of dissolved gas in the catalyst layer seems to originate from  
31 mass transfer limitations during operation [39]. According to Trinke et al., this has been recognised  
32 also as the driving force of gas cross-over [39]. According to Schalenbach et al. [40-41] high  
33 saturations hinder the gas transport and thus lead to an increase of local pressure. This was also  
34 suggested by Bessarabov et al. [42]. Evidence of supersaturation of oxygen in acidic water  
35 electrolysis was further reported by Shibata and Kikuchi et al. [43-44].  
36  
37  
38  
39  
40  
41  
42  
43  
44  
45  
46  
47  
48  
49  
50  
51  
52  
53  
54  
55

56 However, beside all these evidences, another important phenomenon should be considered.  
57 This regards the modification of the oxidation state at the anode catalyst surface, according to the  
58  
59  
60  
61  
62  
63  
64  
65

1  
2  
3  
4  
5  
6  
7  
8  
9  
10  
11  
12  
13  
14  
15  
16  
17  
operating potential window, during the cell switch from OCV (or low current density operation) to  
a high current density electrolysis mode and reverse. It is well-established that oxygen evolution  
reaction (OER) activity is closely linked to the nature of the IrRu-oxide species at the surface and  
an excursion at lower potentials could regenerate the catalyst. When the cell is under OCV, the  
anode is not subjected to highly oxidizing conditions, as during operation, and its oxidation state  
could change. Thus, less oxidising conditions may affect the anode surface and modify its catalytic  
properties.

18  
19  
20  
21  
22  
23  
24  
25  
26  
27  
28  
29  
30  
31  
32  
33  
34  
35  
36  
37  
Literature reports using near ambient pressure X-ray photoelectron spectroscopy for in situ  
monitoring of the surface state of membrane electrode assemblies during water splitting, have  
shown, with particular regard to  $\text{Ir}_{0.7}\text{Ru}_{0.3}\text{O}_2$  anodes, that oxygen evolution occurs through a  
surface Ru(VIII) intermediate [45]. With regard to the iridium catalytic sites, Ir III/IV  
oxides/hydroxides have been detected by operando near-ambient pressure X-ray photoelectron  
spectroscopy on membrane-electrode assemblies [45]. During electrolysis operation, oxidation of  
Ir III appears to leave behind a layer of Ir IV oxides/hydroxides, which dominates the surface  
during the oxygen evolution process [46].

38  
39  
40  
41  
42  
43  
44  
45  
46  
47  
48  
49  
50  
51  
52  
53  
54  
55  
56  
57  
58  
59  
60  
61  
62  
63  
64  
65  
Regarding the Pt/C cathode, during an OCV interval, this is initially in contact with some  
residual hydrogen; but, with progressive exposure to air, it can undergo to a slight oxidation on  
the surface [47] with the occurrence of PtO. However, the main effect on the cell performance  
appears to be produced by a change of the oxidation state at the anode during the rest interval  
being the OER the rate determining step.

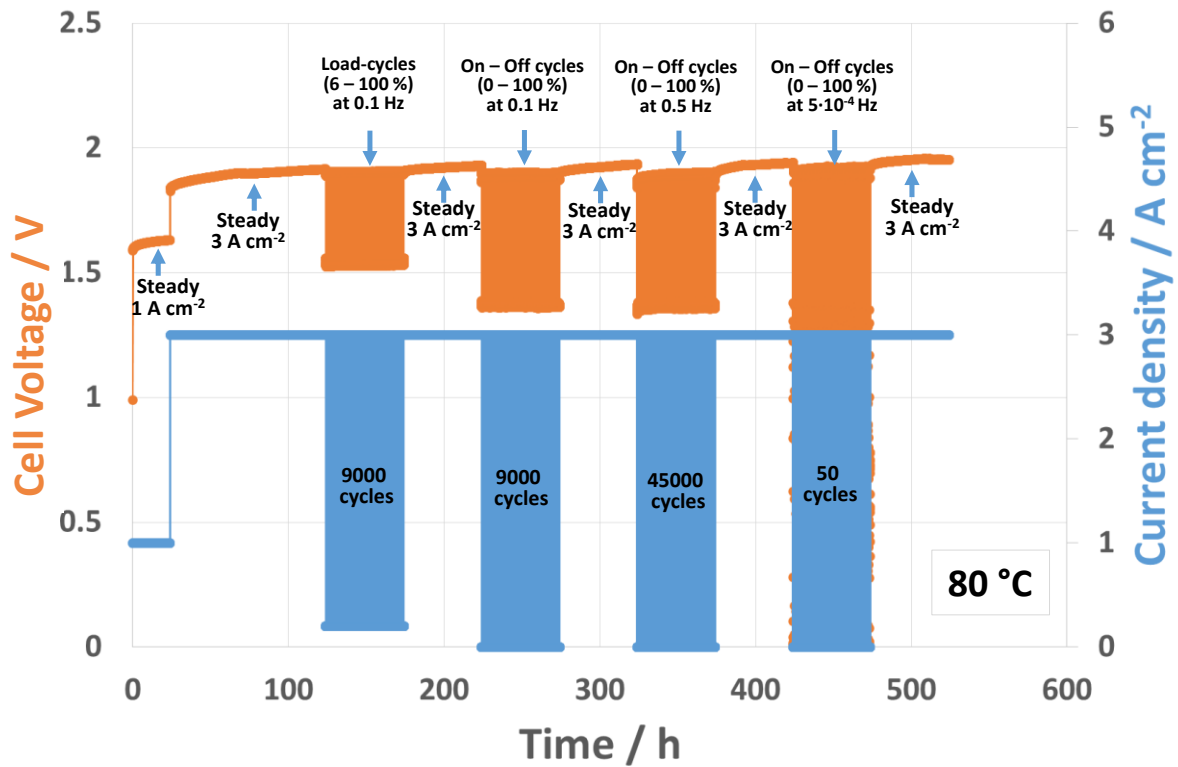


**Fig 3** MEA current density (load) cycles at 80 °C; Pt loading: 0.1  $\text{mg cm}^{-2}$ ;

IrRuOx loading: 0.4  $\text{mg cm}^{-2}$

A current density (load) cycling (530 h) test of the electrolysis single cell, carried out according to the protocol illustrated in Fig. S2, is reported in figure 3. An initial performance decay was observed when the cell was operated at fixed current (Fig. 3), but a lower decay was observed during cycled operation steps both when the minimum load was 6% or 0%. This indicates that a periodic decrease of the operating current density can mitigate performance losses (the cell potential appears to decrease slightly), although it might solely produce a recover of reversible degradation. A lower reversible cell degradation is therefore foreseen during cycled operation in grid balancing service. Interestingly, the **recovery** of reversible losses is larger when the frequency of the cycles and the current density window are increased. After the load cycles, the same MEA was subjected to a combined load and thermal cycles 210 h protocol (between 25°C and 80°C, at different current densities i.e. 1 and 3  $\text{A cm}^{-2}$ ). The results are shown in Fig. 4. No relevant additional performance decay during the procedure combining thermal cycles and current density

cycles was observed. Excluding the first 100 h, the cell voltage increase was about 95  $\mu\text{V}/\text{h}$  during the overall load cycles test and almost 0  $\mu\text{V}/\text{h}$  during the successive thermal/load cycles.

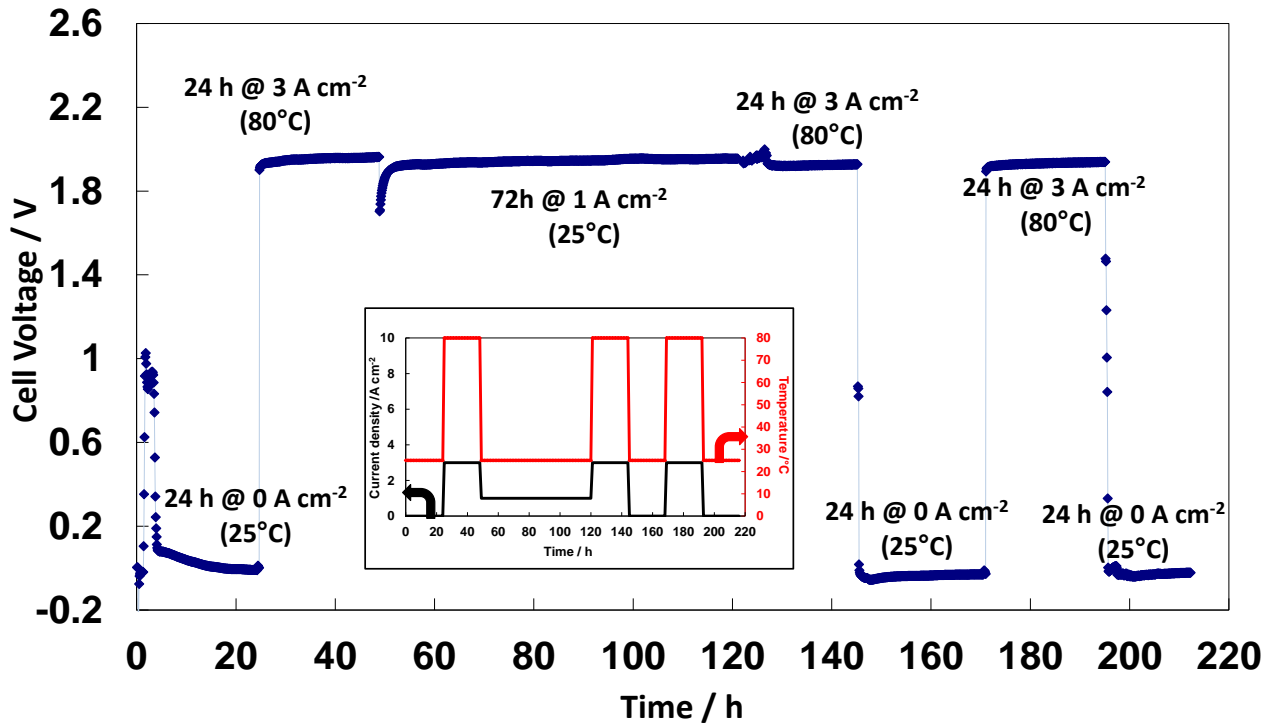
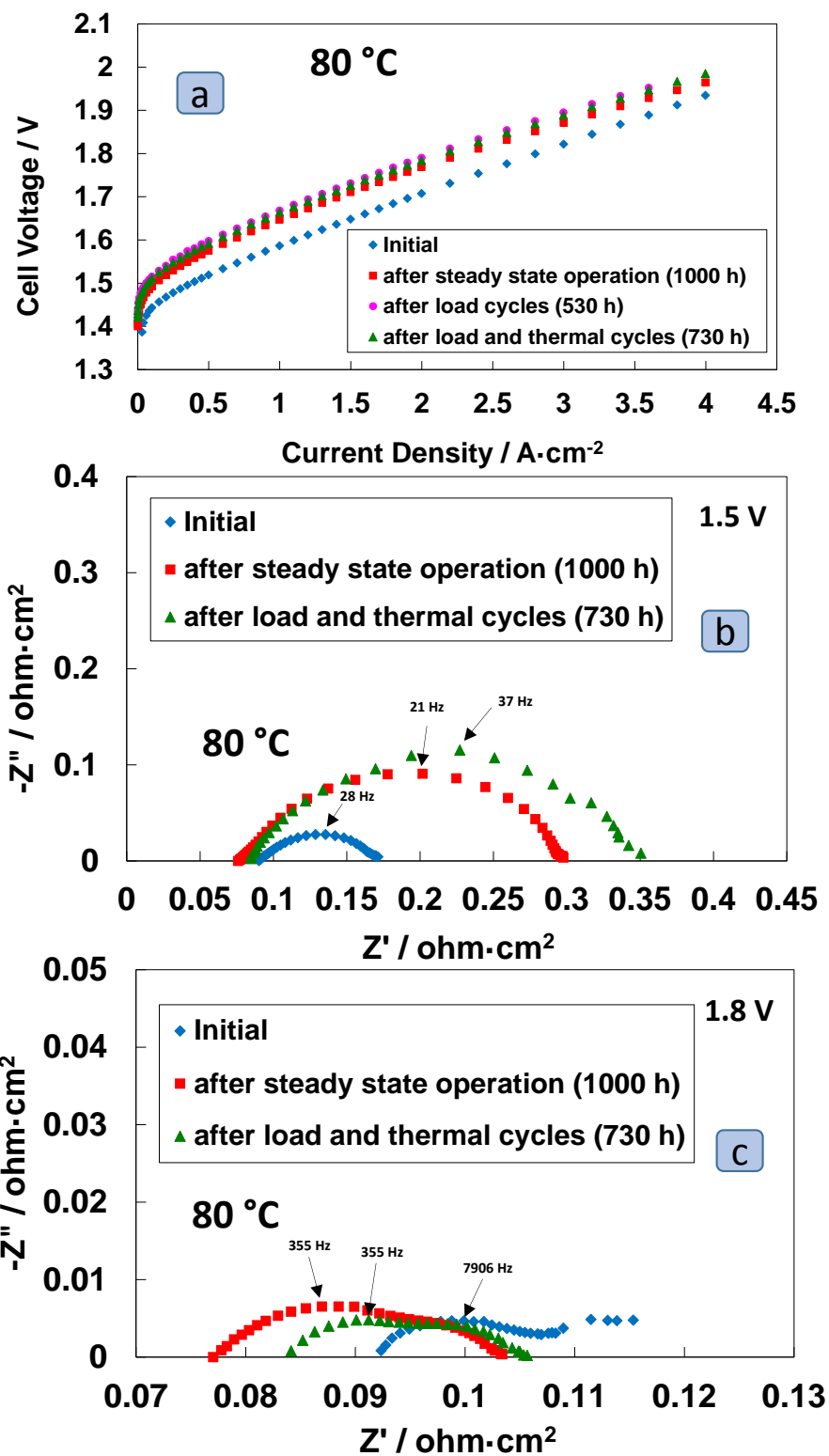


Fig. 4 Temperature and current cycling of the PEM electrolysis MEA; the test protocol is shown in

the inset; Pt loading: 0.1  $\text{mg cm}^{-2}$ ; IrRuOx loading: 0.4  $\text{mg cm}^{-2}$



**Fig. 5** MEA polarization curves (a) and impedance spectroscopy at 1.5 V (b) and 1.8 V (c) before and after steady-state durability and cycle tests; Pt loading: 0.1 mg cm<sup>-2</sup>; IrRuOx loading: 0.4 mg cm<sup>-2</sup>.



1 To confirm data reproducibility in polarization tests, various sets of polarization curves were  
2 carried out under each condition. The standard deviation in the polarization curves was < 5 mV for  
3 each data point of the overall data-set at the beginning of life and < 4 mV after the durability tests.  
4

5  
6  
7 Thus the loss of efficiency associated to the increase of cell voltage appears more evident  
8 during the initial (530 h) load cycles, than in the successive thermal/load cycles (210 h). Moreover  
9 the steep increase of potential upon a current density switch is generally larger when the  
10 temperature is low (25 °C) than at 80 °C. These evidences indicate the occurrence of recoverable  
11 or reversible losses especially at 3 A cm<sup>-2</sup>. Thus, the cell voltage increase is, at some extent, mainly  
12 associated to reversible losses. As discussed above, these are probably arising from mass transfer  
13 issues caused by gas evolution [48-49] or by a modification of the anode oxidation state according  
14 to the specific operating potential window [45-46]. In principle, zero-current intervals or cell shut  
15 down can allow to recover part of the voltage increase. It is considered that upon cell shut down,  
16 the gas molecules entrapped in the catalysts micro-pores can escape leaving the pores empty or  
17 the excursion at lower potential could regenerate the catalyst. Both phenomena, results in much  
18 lower mass transfer or kinetic overpotentials when the current is again switched from 0 to 3 A cm<sup>-2</sup>  
19 . During continuous operation at 3 A cm<sup>-2</sup>, the evolved gas can not escape easily from the pores  
20 because of the occurrence of a supersaturation effect [50] producing an increase of local pressure.  
21 Bessarabov et al. [42] and Schalenbach et al. [40-41] have suggested that high saturations hinder  
22 the gas transport thus leading to an increase of local pressure. This possibly causes an increase of  
23 cell voltage according to the Nernst law [51]. Both phenomena i.e., change of catalytic activity due  
24 to a variation of the catalyst oxidation state and mass transfer issues caused by supersaturation  
25 with an increase of the local pressure may have a different impact in determining the overall  
26 reversible losses. This would require specific studies including in situ spectroscopic analysis to  
27 single out which of these phenomena is the most relevant one.  
28  
29  
30  
31  
32  
33  
34  
35  
36  
37  
38  
39  
40  
41  
42  
43  
44  
45  
46  
47  
48  
49  
50  
51  
52  
53  
54  
55  
56  
57  
58  
59  
60  
61  
62  
63  
64  
65

1 A comparison of the polarization curves and impedance spectra for the fresh MEA and the  
2 MEAs subjected to steady-state operation (1000 h), to load cycles (530 h) and to combined load  
3 and thermal cycles (210 h) is reported in figure 5. An increase of the cell voltage onset after both  
4 steady-state and cycling test procedures, is evident from the polarization curves (Fig. 5a). No  
5 particular difference between 530 h load cycles and the successive combined 210 h load and  
6 thermal cycles is observed. It is pointed out that the combined 210 h thermal-load cycles  
7 procedure has been carried out just after the 530 h load cycles procedure.  
8  
9

10 In general, the cell voltage increase in the polarization curves is slightly larger after the cycling  
11 procedure than after the steady-state operation. The effect is less evident at high current density.  
12 In terms of efficiency, at 3  $\text{A cm}^{-2}$ , the cell voltage in the polarization curves increases by 50 mV  
13 (steady-state) and 70 mV (overall load and thermal cycling) with the respect to the initial value. In  
14 particular, at 3  $\text{A cm}^{-2}$ , the voltage efficiencies with respect to the high heating value (HHV) are 79  
15 % and 78 % after the overall 1000 h steady-state and the total 740 h load and thermal cycles tests,  
16 respectively.  
17  
18

19 The increase of the cell voltage onset after each test is mainly associated to an increase of  
20 polarization resistance at low frequency, quite evident in the impedance spectra at 1.5 V (Fig. 5b).  
21 This increase of cell voltage may be in part associated to a catalyst degradation.  
22  
23

24 Ac impedance analysis at 1.8 V (Fig. 5c) clearly shows a decrease of the series resistance for  
25 both steady-state and load/thermal cycle tests compared to the fresh MEA. This was essentially  
26 due to a slight thinning of the polymer electrolyte membrane as evidenced by post-operation SEM  
27 analysis of the MEA cross section (see below). It is interesting to note that the series resistance of  
28 the MEA operated under fully steady-state condition (1000 h) is lower than that of the MEA  
29 subjected to the cycled operation (740 h). Thus, membrane thinning is essentially affected by the  
30 number of uptime hours at high current density. Moreover, the polarisation resistance at 1.8 V is  
31  
32  
33  
34  
35  
36  
37  
38  
39  
40  
41  
42  
43  
44  
45  
46  
47  
48  
49  
50  
51  
52  
53  
54  
55  
56  
57  
58  
59  
60  
61  
62  
63  
64  
65

1 smaller for the MEA operated under cycling conditions than under steady-state. This result does  
2 not appear to be aligned to the impedance response at 1.5 V where the polarisation resistance is  
3 larger after the cycles. However, it should be pointed out that the spectra at 1.5 V reflect the  
4 activation region and thus the catalyst behaviour mainly. Whereas at 1.8 V (high current density  
5 region) both reaction kinetics and mass transfer issues are reflected in the ac-impedance  
6 response. Two semicircles are clearly observed at 1.8 V. The one at low frequency is usually  
7 affected by mass transport issues [52]. This second semicircle is more evident in the ac-impedance  
8 spectra of the MEAs subjected to durability studies compared to the fresh MEA (Fig. 5c).  
9 Moreover, comparing the MEA subjected to dynamic operation and the one operated under  
10 steady-state conditions, the low frequency semicircle is more relevant in the latter one. At high  
11 current density, the diffusion constraints related to the evolution of the produced gases are more  
12 critical when continuous electrolysis operation is applied. On the other hand, during the cycles  
13 protocol, when lower or no electrical current is applied, the MEA can in principle recover part of  
14 the reversible losses occurred during the previous electrolysis operation period at high current  
15 density. In other words, the gases entrapped in the catalyst micro-pores can have sufficient time  
16 during the rest interval between two high current density steps to escape. Thus, at the beginning  
17 of a new electrolysis step at high current density, after a rest interval, a lower hindering effect  
18 towards gas evolution occurs until the gas is re-accumulated again in the micro-pores.

19 The significant decrease of the cell series resistance at 1.8 V in the MEA that has operated  
20 under steady-state for 1000 h, compensates for the large polarisation losses which appear critical  
21 under continuous operation at high current density (Fig. 5c). Thus, the overall impedance is slightly  
22 larger after the cycled operation compared to the fully steady-state test. At 1.8 V, the shift of the  
23 series resistance to lower values for the used MEAs compared to the fresh MEA causes an overall  
24 impedance (low frequency intercept) in the latter slightly higher than the used MEAs. This

1 corresponds to a higher differential resistance at high currents (3-4 A cm<sup>-2</sup>). Accordingly, at high  
2 current density, the slope of the polarization curves is higher in the case of the fresh MEA with  
3 respect to the used MEAs (Fig. 5a).  
4  
5

6  
7 However, being the overall impedance of the used MEAs at 1.5 V much higher than the fresh  
8 MEA, their cell voltage increase in the activation region (e.g. until 0.2 A cm<sup>-2</sup>) is significantly larger.  
9  
10 This reflects on the overall polarization curves, not in terms of slope but in terms of overall cell  
11 voltage increase. By comparing the impedance spectra at 1.5 and 1.8 V, one can say that, on a  
12 comparable time scale (1000 vs. 740 h), the cycles have a major impact on catalyst degradation  
13 whereas the steady state operation causes larger reversible losses and more membrane thinning  
14 effect.  
15  
16  
17  
18  
19  
20  
21  
22  
23  
24

### 25 3.2 Morphological and surface characterization

26  
27 To better understand the degradation mechanisms, ex-situ post-operation analyses were  
28 carried out on a fresh MEA and used MEAs. Scanning electron microscopy (SEM) of the MEAs  
29 cross-sections are reported in Figure 6. A good adhesion of the electrodes to the membrane was  
30 observed in both fresh and used MEAs (Fig. 6a-c). However, the SEM cross-sections of the used  
31 MEAs show some loss of the outer anode catalyst layers (Fig. 6b). This because some outer anode  
32 layers of the used MEAs were in part transferred to the diffusion layer backing (Ti mesh) in contact  
33 with the anode during the disassembly of the cell. Whereas the cathode layer that was in contact  
34 with the carbon-based GDL was not affect by the disassembling procedure. No significant change  
35 in the morphology of the catalytic layers was recorded both after the steady-state and load  
36 and thermal cycles tests. A slight thinning of the membrane was evident after both durability tests,  
37 with the MEA operated under steady-state conditions showing the thinnest membrane. This was  
38 in agreement with the observed series resistance decrease in the impedance spectra (Figs. 5b-c).  
39  
40  
41  
42  
43  
44  
45  
46  
47  
48  
49  
50  
51  
52  
53  
54  
55  
56  
57  
58  
59  
60  
61  
62  
63  
64  
65

subjected to load and thermal cycles and to  $81 \pm 3 \mu\text{m}$  in the MEA operated under steady-state conditions (Fig. 6a-c).

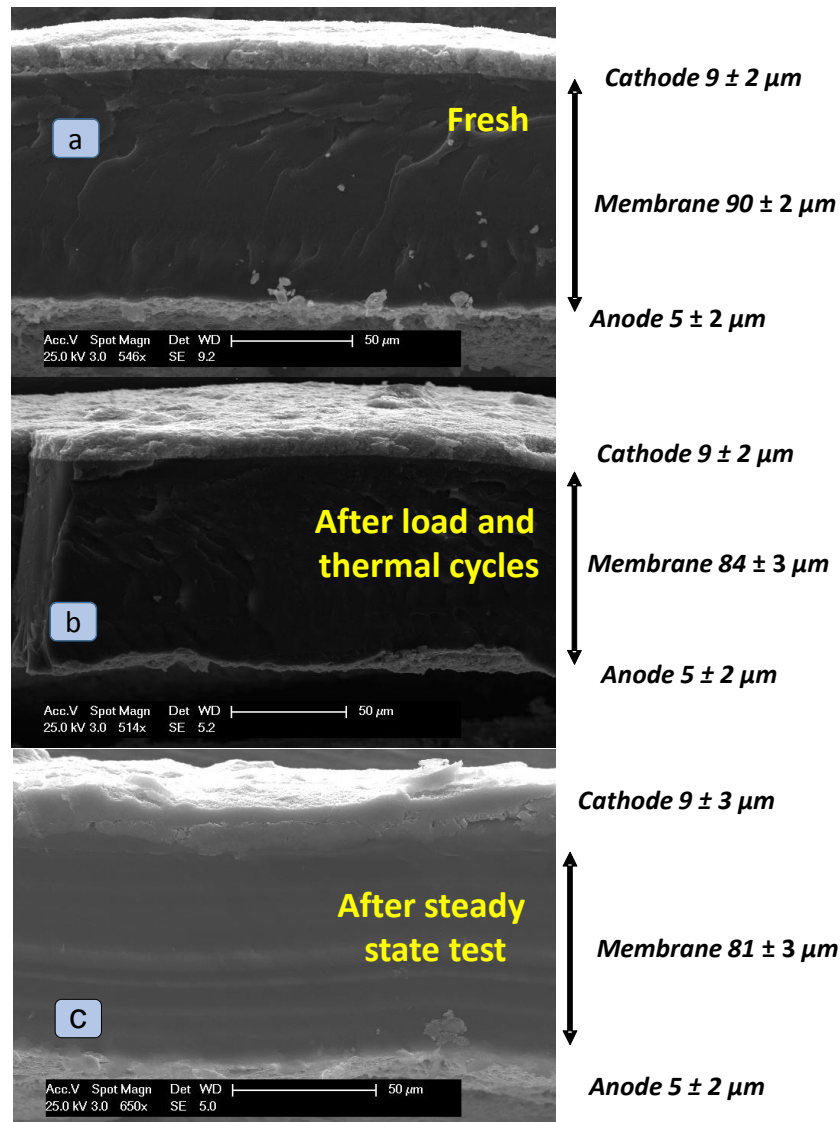


**Fig. 6** SEM Cross-sections of fresh (a) and used MEAs subjected (b) to combined 740 h load and thermal cycles (c) and to 1000 h steady-state electrolysis operation (the cathode layer is shown on the top for all MEAs)

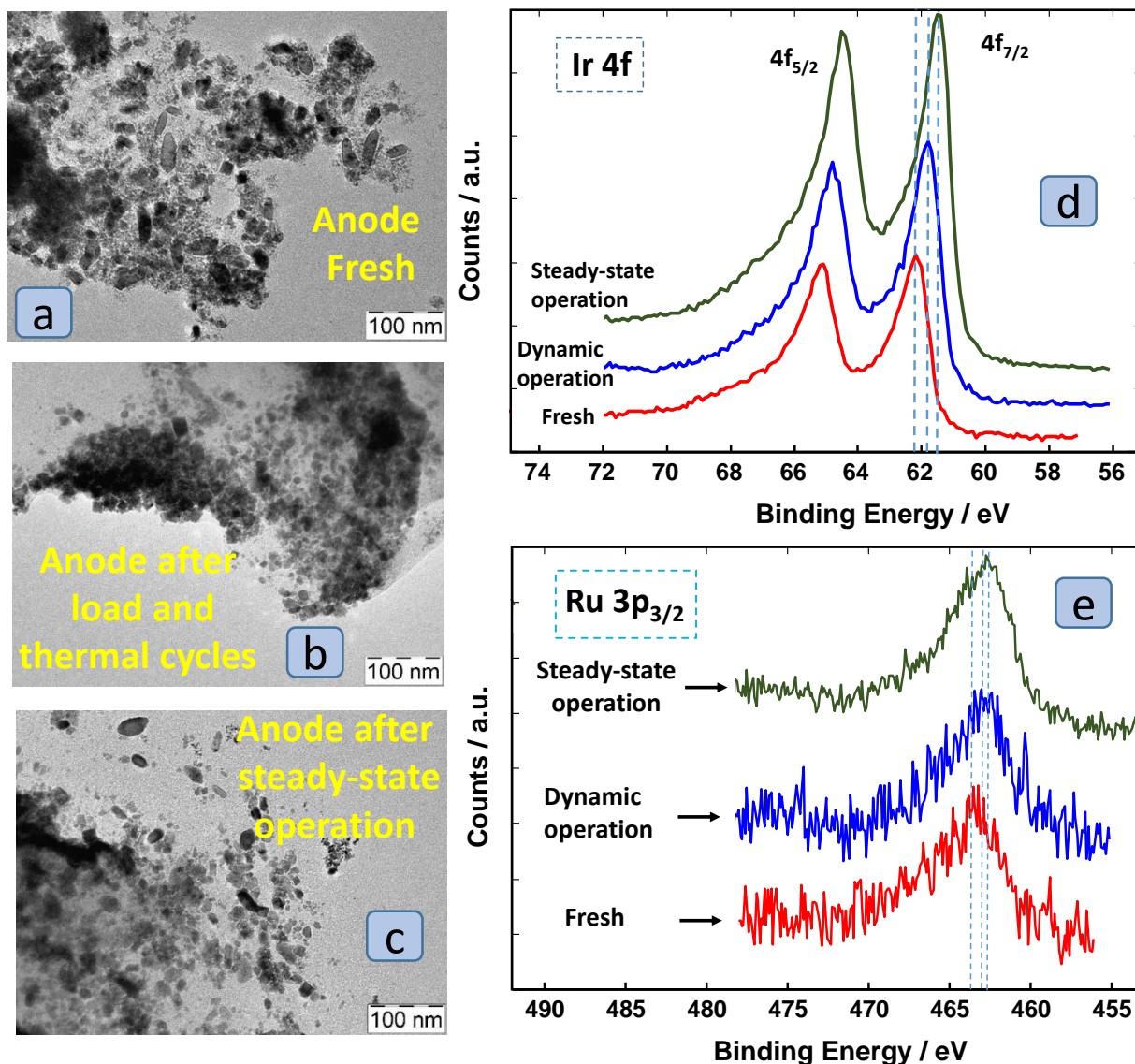


**Fig. 7** TEM images for the fresh anode (a), the anode after 740 h load and thermal cycles (b), and the anode after 1000 h steady-state operation (c); high resolution Ir 4f (d) and Ru 3p<sub>3/2</sub> (e) XPS analyses before and after the 740 h combined electrolysis cycling tests (dynamic operation) and 1000 h steady-state operation.

Figure 7a-c shows the TEM images of the anode layer for fresh and used MEAs. The anode was composed of both IrRu-oxide nanoparticles and Aquivion ionomer. The IrRu-oxide anode morphology shows a mixture of nanosized irregularly shaped and faceted particles (Fig. 7a). For what concerns the faceted particles, squared and rectangular (rod-like) shape nanocrystals are

quite evident. The ionomer is well evident in the used samples. After the cycling test, the anode layer appears to be slightly less agglomerated than in the case of the fresh anode. Probably the reaction interface was extended by cycled electrolysis operation (infiltration of ionomer inside the catalyst agglomerates) as also observed after the steady-state operation. This phenomenon has been also observed in previous durability tests [26]. Post operation analysis of similar PEM MEAs subjected to steady-state tests and the related degradation mechanisms have been reported in previous works [25, 26].

XPS analysis was carried out on the anodic surface of a fresh MEA and used MEAs. Fig. 7d-e compares fresh and used MEAs. The Ir4f and Ru3p<sub>3/2</sub> photoelectron lines were selected for qualitative and quantitative analysis of the relative surface concentrations of Ir and Ru (Table 1). By comparing the B.E. of Ir 4f peaks, a shift to lower B. E. upon both steady-state operation and thermal and load cycling is quite evident (Fig. 7d). The shift of Ir 4f towards lower B.E. is more relevant for the MEA operated under steady-state than the one operated under dynamic mode (Fig. 7d).

A detailed analysis of the Ir 4f region (Fig. 7d; Fig. S5a-c, Table S1) indicates an increasing occurrence of sub-stoichiometric Ir<sup>3+</sup> species for the anode surface upon 1000 h steady-state operation and 730 h cycling. This could be due to the presence, in the used sample, of iridium sites having unsaturated coordination with oxygen species; in other words, a sub-stoichiometric Ir-oxide is formed upon both steady-state operation and cell cycling. Whereas the Ir signal of the fresh anode shows a higher binding energy, entirely corresponding to Ir<sup>4+</sup> in the IrO<sub>2</sub> structure compared to the used anodes. Fig. S5a-c provides a comparison of the deconvoluted Ir 4f spectra for all the three MEAs here investigated i.e. fresh MEA and used MEAs. The occurrence of an increased concentration of Ir<sup>3+</sup> species, at lower binding energies, in both used MEAs compared to

1  
2  
3  
4  
5  
6  
7  
8  
9  
10  
11  
12  
13  
14  
15  
16  
17  
18  
19  
20  
21  
22  
23  
24  
25  
26  
27  
28  
29  
30  
31  
32  
33  
34  
35  
36  
37  
38  
39  
40  
41  
42  
43  
44  
45  
46  
47  
48  
49  
50  
51  
52  
53  
54  
55  
56  
57  
58  
59  
60  
61  
62  
63  
64  
65

the fresh MEA is confirmed. In fact, an additional peak at lower B.E. occurs upon operation; this peak is larger in intensity after continuous operation compared to the dynamic mode.

A shift of Ru3p<sub>3/2</sub> peak to lower binding energy for the used anodes is also evident (Fig. 7e, S6). Thus, the same phenomena occurring for Ir, are also registered for the Ru sites present on the surface of the used sample (Table 1).

It is derived that both electrolysis cycles and prolonged steady operation can cause an extraction of oxygen from the Ir-Ru-oxide with the formation of a substoichiometric Ir-Ru oxide phase on the surface [25, 26]. The atomic Ir/Ru ratio on the surface slightly varied upon cycling from 75 at. % Ir and 25 at. % Ru in the fresh anode to 80 at. % Ir and 20 at. % Ru after cycled operation whereas this metal ratio did not change substantially after the steady-state operation (Table 1) in accordance with what observed in our previous durability tests [25, 26]. A bulk energy dispersive X-ray analysis (Table 1) also shows a slight loss of Ru from the anode operated under dynamic mode (a typical EDX spectrum of the cycled anode is shown in Fig. S7). Beside the presence of a sub-stoichiometric oxide phase on the anode surface, the slight loss of Ru species may represent another cause of catalyst performance degradation especially associated to cycled operation as observed in the impedance spectra collected in the activation region of the polarisation curves (Fig. 5b).

TEM images of the cathode layer for the fresh and cycled MEAs are reported in Fig. 8a-c. The Pt/C catalysts are embedded into the Aquivion® ionomer layer. A very slight growth of the Pt particles upon cycled operation is observed. Similar evidence is observed after the steady-state test (Table 1). However, although this slight cathode sintering may contribute to some catalyst performance degradation, the degradation phenomena observed for the anode appear more relevant being this process the rate determining step in the activation region [44]. The anode



degradation is essentially considered the **main** responsible of the increase of polarization resistance in the low cell voltage region.

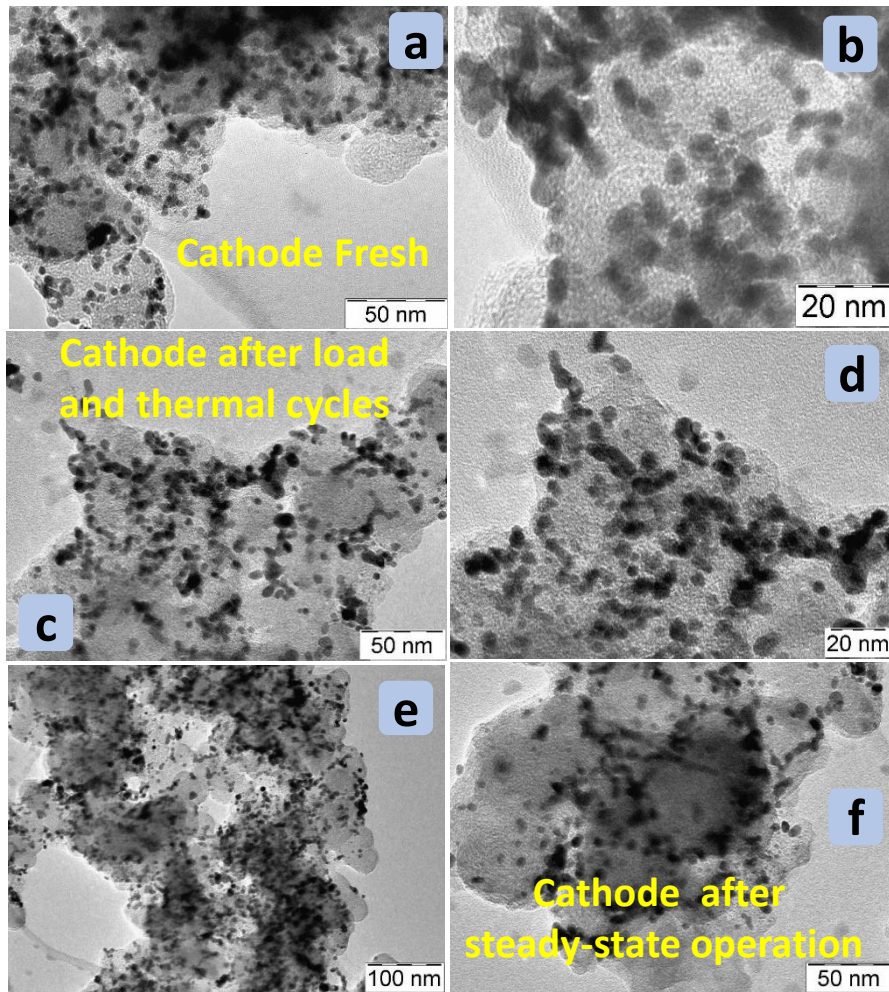


**Fig. 8** TEM images for the fresh MEA cathode (a-b), the MEA cathode after 740 h load and thermal cycles (c-d), and the MEA cathode after 1000 h steady-state durability test (e-f).

The results of the ex-situ physico-chemical analyses are summarised in Table 1. The main changes, observed for the used MEAs compared to the fresh one, are a slight thinning of the membrane and the presence of substoichiometric oxide species at the anode. Both phenomena are more evident after the steady-state durability test. Both bulk and surface elemental compositions (EDX and XPS analyses, respectively) for the metals involved in the anode do not vary significantly after the steady-state operation but some losses of Ru are envisaged after the dynamic operation. The

mean catalyst particle size appears not much affected by the durability tests for the anode and just in a modest extent for the cathode.

**Table 1.** Survey of main results from ex-situ physicochemical analysis

Units	Membrane thickness $\mu\text{m}$	Bulk elemental analysis of Ir and Ru metals in the anode layer SEM-EDX		Surface elemental analysis of Ir and Ru metals in the anode layer XPS		B.E. Ir $4f_{7/2}$	B.E. Ru $3p_{3/2}$	Mean particle size anode	Mean particle size cathode
		Ir at. %	Ru at. %	Ir at. %	Ru at. %	eV	eV	nm	nm
FRESH MEA	$90 \pm 2$	$70.1 \pm 0.5$	$29.9 \pm 0.5$	$75.4 \pm 2.0$	$24.6 \pm 2.0$	62.18	463.48	$6 \pm 2.0$	$2.5 \pm 0.5$
MEA operate in steady-state mode	$81 \pm 3$	$70.7 \pm 0.5$	$29.3 \pm 0.5$	$76.2 \pm 2.0$	$23.8 \pm 2.0$	61.50	462.67	$6 \pm 2.0$	$3.0 \pm 0.5$
MEA operated with load and thermal cycles	$84 \pm 3$	$76.7 \pm 0.5$	$23.3 \pm 0.5$	$80.3 \pm 2.0$	$19.7 \pm 2.0$	61.82	462.84	$5 \pm 2.0$	$3.5 \pm 0.5$

In a recent article [53], the main degradation mechanisms for proton exchange membrane electrolyzers have been reviewed. These mechanisms appear to be accelerated by specific stressors such as high current density, dynamic operation, and shutdown modes. Yet, most of the previous degradation studies, dealing with dynamic mode, have mainly regarded operation at current densities up to  $1\text{-}2 \text{ A cm}^{-2}$  and using MEAs containing high precious metal catalyst loadings ( $2\text{-}3 \text{ mg cm}^{-2}$ ). The main degradation mechanisms for these operating conditions are associated with anode catalyst dissolution, membrane chemical decomposition, and formation of semiconducting oxides on the metal components.

Rakousky et al have investigated PEM electrolysis cell operation up to  $3 \text{ A cm}^{-2}$  but using high catalyst loadings of  $3 \text{ mg PGM cm}^{-2}$  [24]. At elevated current densities, two primary factors have been identified to cause performance degradation, i.e. the increase in ohmic cell resistance and

1 the appearance of mass-transport resistance [24]. Both aspects appeared to contribute to the  
2 voltage increase in equal measure [24].  
3

4  
5 Of course, operation at higher currents in combination with much lower catalyst loadings,  
6  
7 corresponding to significantly higher turnover frequencies [25], as in the present case, introduces  
8  
9 new aspects, such as an increase of recoverable losses effects associated with catalyst  
10  
11 modifications and mass transfer issues as well as an increase of irreversible degradation mainly  
12  
13 affecting the anode catalyst.  
14  
15

16  
17  
18 The aim of this work was thus to understand if, under these specific conditions of high current  
19  
20 density and low PGM loading, the dynamic operation could affect cell degradation in a much more  
21  
22 relevant way compared to the continuous operation. This does not seem the case according to  
23  
24 both the results of durability studies and post-operation analyses. Such evidences are in  
25  
26 agreement with the literature reports for large catalyst loaded MEAs [22] showing that dynamic  
27  
28 operation does not enhance significantly the degradation in the case of high PGM loadings and  
29  
30 mild operating current densities. Even if, it has been observed that the dynamic mode may cause  
31  
32 relevant membrane thinning [22]. In our case, we have evidence that the uptime hours at high  
33  
34 current density are more relevant in determining membrane thinning than the dynamic operation.  
35  
36 However, it is important to consider that this phenomenon is very much depending on the degree  
37  
38 of stabilisation of the membrane consequent to its associated post-fluorination treatment.  
39  
40  
41

42  
43  
44 In general, it appears that, although similar degradation mechanisms are identified for most of the  
45  
46 investigated PEM electrolysis devices, the impact of each mechanism can vary according to the  
47  
48 operating conditions, i.e. current density, operation mode (dynamic or continuous), catalyst  
49  
50 loading, membrane thickness and stabilisation treatment, and type of cell configuration including  
51  
52 porous transport layers, bipolar plates etc. Degradation can also vary significantly in different  
53  
54 regions of the MEA according to the specific cell design [54].  
55  
56  
57  
58  
59  
60

1 Different operation strategies require specific analyses to identify the factors that can have the  
2 main influence in determining the life-time of a PEM electrolysis device.  
3

## 4 **Conclusions**

5  
6  
7 The effects of high frequency and high current density ( $3 \text{ A cm}^{-2}$ ) load cycling, as well as thermal  
8 cycling, on the degradation of low metal catalyst loading-based MEAs ( $0.44 \text{ mg}_{\text{PGM}} \text{ cm}^{-2}$ ) have  
9 been here investigated. Previous literature reports have mainly dealt with understanding the  
10 degradation mechanisms of high precious metal loading-based MEAs operated under at moderate  
11 current densities. However, dynamic operation at high frequency and high current density for low  
12 catalyst loading MEAs is of relevant interest to decrease capital costs and to better understand the  
13 grid balancing service (grid stabilisation, peak shaving etc.) characteristics of next generation  
14 electrolyzers. Electrolysis operation under such harsh conditions can in principle exacerbate MEA  
15 degradation thus decreasing the impact of the specific advantages.  
16  
17  
18  
19  
20  
21  
22  
23  
24  
25  
26  
27  
28  
29  
30

31 It was observed that the smaller cell voltage increases for the low PGM loaded MEA operated  
32 continuously at high current density compared to the same MEA subjected to dynamic mode was  
33 essentially related to a larger decrease of series resistance during operation. This effect was  
34 associated to a larger membrane thinning during the steady-state mode compared to the cycled  
35 operation. Such phenomenon compensates for a larger increase of polarization resistance  
36 associated to mass transfer issues, at high current density, under continuous operation.  
37  
38  
39  
40  
41  
42  
43  
44  
45

46 Accordingly, it is expected that, in the case of membranes properly stabilized to sustain  
47 operation at high currents without thinning effects, the cell voltage increase caused by load cycles  
48 would not be higher than that recorded during the steady-state operation. The main differences  
49 observed between these two different operating modes are that load cycling can exacerbate  
50 catalyst degradation while continuous operation causes larger recoverable losses and polymer  
51 electrolyte thinning. On the other hand, under some circumstances, load cycles can play a  
52  
53  
54  
55  
56  
57  
58  
59  
60  
61  
62  
63  
64  
65

1 temporary positive effect, at least in terms of catalyst regeneration and/or reduction of mass  
2 transfer issues at high current density (refresh cycles).  
3

4  
5 It appears that, in a durability study, keeping the cell at zero current for sufficient times can  
6 allow to recover part of the reversible losses. This aspect may involve two different phenomena,  
7 i.e., excursion at lower potentials could regenerate the catalyst by changing the oxidation state on  
8 the surface according to the different potential window and/or allowing the gas molecules  
9 entrapped in the micro-pores to escape from the catalyst layer. The latter phenomenon can  
10 reduce the gas supersaturation in the catalytic layer with a consequent gain in efficiency in the  
11 subsequent electrolysis step. The occurrence of a second semicircle in the low frequency range of  
12 the ac-impedance spectra obtained at high currents would corroborate the mass transfer issues  
13 mechanism. In fact, this semicircle is more evident under the conditions where recoverable losses  
14 occur at larger extent (steady-state operation). However, a partial recover of reversible losses is  
15 also observed during load cycling at high frequency that is more compatible with a change of the  
16 anode catalyst oxidation state. Possibly both mechanisms (escape of gases entrapped in the  
17 micropores and catalyst surface regeneration at low current densities) may occur during such  
18 current switches and appear beneficial for recovering voltage losses.  
19  
20  
21  
22  
23  
24  
25  
26  
27  
28  
29  
30  
31  
32  
33  
34  
35  
36  
37  
38  
39  
40

41 Beside recoverable losses, irreversible catalyst degradation is causing an increase of  
42 polarization resistance in the activation region for the used MEAs. This is slightly larger for the  
43 cycled MEA compared to the MEA operated in a steady-state test. Formation of substoichiometric  
44 IrRu-oxide on the surface of the used MEAs appears to be one of the main degradation factors  
45 accounting for irreversible catalyst degradation during operation at high current density beside  
46 the loss of Ru species especially observed after dynamic operation. The impact on catalyst  
47 degradation caused by the substoichiometric oxide phase occurrence at the anode surface, upon  
48 prolonged operation, appears slightly lower than the loss of Ru species. In fact, the increase of  
49  
50  
51  
52  
53  
54  
55  
56  
57  
58  
59  
60  
61  
62  
63  
64  
65

1 polarization resistance in the activation region of the polarisation curve is slightly more relevant in  
2 the case of cycled operation where Ru losses are identified. Interestingly no relevant growth of the  
3 nanosized catalyst particles is observed.  
4  
5

6  
7 The acquired knowledge may be helpful in designing more stable MEAs for operation under  
8 such harsh dynamic operating conditions by focusing on stabilised membranes, robust solid  
9 solutions of Ir and Ru oxides with tailored core-shell structures and enhanced morphologies for  
10 the catalyst layers.  
11  
12  
13  
14  
15  
16  
17  
18  
19

## 20 **Acknowledgements**

21  
22  
23 CNR-ITAE authors acknowledge the financial support from the NEPTUNE project. This project has  
24 received funding from Fuel Cells and Hydrogen 2 Joint Undertaking under grant agreement No  
25 779540. This Joint Undertaking receives support from the European Union's Horizon 2020 research  
26 and innovation programme and Hydrogen Europe and Hydrogen Europe Research.  
27  
28  
29  
30  
31  
32  
33  
34  
35

## 36 **References**

- 37  
38 [1] [https://eur-lex.europa.eu/legal-content/EN/TXT/?uri=celex:22016A1019\(01\)](https://eur-lex.europa.eu/legal-content/EN/TXT/?uri=celex:22016A1019(01))  
39  
40  
41 [2] A.S. Aricò, S. Siracusano, N. Briguglio, V. Baglio, A. Di Blasi, V. Antonucci, J Appl Electrochem 43  
42 (2013) 107–118  
43  
44  
45 [3] M. Carmo, D.L. Fritz, J. Mergel, D. Stolten, Int. J. Hydrogen Energy. 38 (2013) 4901–4934.  
46  
47  
48 [4] PEM Water Electrolysis, Pierre Millet, chapter 3, Hydrogen Production: Electrolysis book,  
49 Editor: Agata Godula-Jopek, First published:6 February 2015, Print ISBN:9783527333424; Online  
50 ISBN:9783527676507; DOI:10.1002/9783527676507;  
51  
52  
53  
54  
55  
56  
57 <https://doi.org/10.1002/9783527676507.ch3>  
58  
59 [5] Q. Feng, X.-Z. Yuan, G. Liu, B. Wei, Z. Zhang, H. Li, Ha. Wang, J. Power Sources 366 (2017) 33-55  
60  
61  
62  
63  
64  
65

- 1  
2  
3  
4  
5 [6] J.A. Staser, J.W. Weidner, Effect of water transport on the production of hydrogen and sulfuric  
6 acid in a PEM electrolyzer, *J. Electrochem. Soc.* 156 (2009).  
7  
8 [7] N. Briguglio, G. Brunaccini, S. Siracusano, N. Randazzo, G. Dispenza, M. Ferraro, R. Ornelas, A.S.  
9 Aricò, V. Antonucci, *Int. J. Hydrogen Energy*. 38 (2013) 11519–11529.  
10  
11 [8] D. Saebea, Y. Patcharavorachot, V. Hacker, S. Assabumrungrat, A. Arpornwichanop, S.  
12 Authayanun, *Chem. Eng. Trans.* 57 (2017) 1615–1620.  
13  
14 [9] G. Chisholm, L. Cronin, M.D. Symes, *Electrochim. Acta.* 331 (2020).  
15  
16 [10] C. Immerz, M. Schweins, P. Trinke, B. Bensmann, M. Paidar, T. Bystroň, K. Bouzek, R. Hanke-  
17 Rauschenbach, *Electrochim. Acta.* 260 (2018) 582–588.  
18  
19 [11] A.C. Olesen, S.H. Frensch, S.K. Kær, *Electrochim. Acta.* 293 (2019) 476–495.  
20  
21 [12] S.H. Frensch, A.C. Olesen, S.S. Araya, S.K. Kær, *Electrochim. Acta.* 263 (2018) 228–236.  
22  
23 [13] P. Millet, N. Mbemba, S.A. Grigoriev, V.N. Fateev, A. Aukauloo, C. Etiévant, *Int J Hydrogen*  
24 *Energy* 36 (2011) 4134-4142.  
25  
26 [14] P. Millet, R. Ngameni, S.A. Grigoriev, N. Mbemba, F. Brisset, A. Ranjbari, C. Etiévant, *Int J*  
27 *Hydrogen Energy* 35 (2010) 5043-5052.  
28  
29 [15] P. Millet, A. Ranjbari, F. De Guglielmo, S.A. Grigoriev, F. Auprêtre, *Int. J. Hydrogen Energy*, 37  
30 (2012) 17478-17487.  
31  
32 [16] S.A. Grigoriev, V.I. Poremskiy, S.V. Korobtsev, V.N. Fateev, F. Auprêtre, P. Millet, *Int. J.*  
33 *Hydrogen Energy*. 36 (2011) 2721–2728.  
34  
35 [17] S.A. Grigoriev, P. Millet, S.V. Korobtsev, V.I. Poremskiy, M. Pepic, C. Etievant, C. Puyenchet,  
36 V.N. Fateev, *Int. J. Hydrogen Energy*, 34 (2009) 5986-5991.  
37  
38 [18] P. Lettenmeier, S. Kolb, F. Burggraf, A.S. Gago, K.A. Friedrich, *J Power Sources* 311 (2016) 153-  
39 158  
40  
41  
42  
43  
44  
45  
46  
47  
48  
49  
50  
51  
52  
53  
54  
55  
56  
57  
58  
59  
60  
61  
62  
63  
64  
65

- 1  
2  
3  
4  
5  
6  
7  
8  
9  
10  
11  
12  
13  
14  
15  
16  
17  
18  
19  
20  
21  
22  
23  
24  
25  
26  
27  
28  
29  
30  
31  
32  
33  
34  
35  
36  
37  
38  
39  
40  
41  
42  
43  
44  
45  
46  
47  
48  
49  
50  
51  
52  
53  
54  
55  
56  
57  
58  
59  
60  
61  
62  
63  
64  
65
- [19] P. Lettenmeier, L. Wang, U. Golla-Schindler, P. Gazdzicki, N.A. Cañas, M. Handl, R. Hiesgen, S.S. Hosseiny, A.S. Gago, K.A. Friedrich, *Angew. Chem. Int. Ed.* 55 (2) (2016) 742-746.
- [20] A.S. Gago, S.A. Ansar, B. Saruhan, U. Schulz, P. Lettenmeier, N.A. Cañas, P. Gazdzicki, T. Morawietz, R. Hiesgen, J. Arnold, K.A. Friedrich, *J Power Sources* 307 (2016) 815-825
- [21] S. Sun, Z. Shao, H. Yu, G. Li, B. Yi, *J Power Sources* 267 (2014) 515-520
- [22] S. H. Frensch, F. Fouda-Onana, G. Serre, D. Thoby, S. S. Araya, S. K. Kær, *Int J Hydrogen Energy* 44 (2019) 29889-29898
- [23] C. Rakousky, U. Reimer, K. Wippermann, S. Kuhri, M. Carmo, W. Lueke, D. Stolten, *J. Power Sources* 342 (2017) 38-47
- [24] C. Rakousky, G. P. Keeley, K. Wippermann, M. Carmo, D. Stolten, *Electrochim. Acta* 278 (2018) 324-331
- [25] S. Siracusano, N. Hodnik, P. Jovanovic, F. Ruiz-Zepeda, M. Šala, V. Baglio, A. S. Aricò, *Nano Energy* 40 (2017) 618-632.
- [26] S. Siracusano, V. Baglio, N. Van Dijk, L. Merlo, A.S. Aricò, *Applied Energy* 192 (2017) 477-489
- [27] S. Siracusano, V. Baglio, A. Stassi, L. Merlo, E. Moukheiber, A.S. Aricò, *Journal of Membrane Science* 466 (2014) 1-7
- [28] S. Siracusano, C. Oldani, M. A. Navarra, S. Tonella, L. Mazzapioda, N. Briguglio, A. S. Aricò, *Journal of Membrane Science* 578 (2019) 136-148
- [29] S. Siracusano, V. Baglio, E. Moukheiber, L. Merlo, A.S. Aricò, *Int J Hydrogen Energy* 40 (2015) 14430-14435.
- [30] A. Ghielmi, P. Vaccarone, C. Troglia, V. Arcella, *J Power Sources* 145 (2005) 108-115.
- [31] A. Stassi, I. Gatto, E. Passalacqua, V. Antonucci, A.S. Aricò, L. Merlo, C. Oldani, E. Pagano, *J Power Sources* 196 (2011) 8925-8930.



1  
2  
3  
4  
5  
6  
7  
8  
9  
10  
11  
12  
13  
14  
15  
16  
17  
18  
19  
20  
21  
22  
23  
24  
25  
26  
27  
28  
29  
30  
31  
32  
33  
34  
35  
36  
37  
38  
39  
40  
41  
42  
43  
44  
45  
46  
47  
48  
49  
50  
51  
52  
53  
54  
55  
56  
57  
58  
59  
60  
61  
62  
63  
64  
65

[32] A. Skulimowska, M. Dupont, M. Zaton, S. Sunde, L. Merlo, D.J. Jones, J. Rozière, *Int J Hydrogen Energy* 39 (2014) 6307-6316.

[33] S. Siracusano, N. Van Dijk, E. Payne-Johnson, V. Baglio, A.S. Aricò, *Appl Catal B* 164 (2015) 488–495.

[34] E. Mayousse, F. Maillard, F. Fouda-Onana, O. Sicardy, N. Guillet, *Int J Hydrogen Energy* 36 (2011) 10474 - 10481

[35] L. Wang, V.A. Saveleva, S. Zafeiratos, E.R. Savinova, P. Lettenmeier, P. Gazdzicki, A.S. Gago, K.A. Friedrich, *Nano Energy*, 34 (2017) 385-391.

[36] A.S. Aricò, A. Stassi, E. Modica, R. Ornelas, I. Gatto, E. Passalacqua, et al, *J Power Sources* 178 (2008) 525-536.

[37] HPEM2GAS project, <https://cordis.europa.eu/project/id/700008/it>; <https://hpem2gas.eu/>

[38] S. Siracusano, N. Van Dijk, R. Backhouse, L. Merlo, V. Baglio, A.S. Aricò, *Renewable Energy* 123 (2018) 52-57

[39] P. Trinke, B. Bensmann, R. Hanke-Rauschenbach, *Int J Hydrogen Energy* 42 (2017) 14355-14366.

[40] M. Schalenbach, M. Carmo, D. L. Fritz, J. Mergel, D. Stolten, *Int J Hydrogen Energy* 38 (2013) 14921-14933

[41] M. Schalenbach, *Int J Hydrogen Energy* 38 (2016) 729-732

[42] D. Bessarabov, A. J. Kruger, S. M Luopa, J. Park, A. A. Molnar, K. A. Lewinski, *ECS Transactions*, 75 (14) (2016) 1165-1173

[43] S. Shibata *Electrochimica Acta* 23 (1978) 619-623

[44] K. Kikuchi, A. Ioka, T. Oku, Y. Tanaka, Y. Saihara, Z. Ogumi, *J Colloid Interface Sci* 329 (2009) 306-309

1  
2  
3  
4  
5  
6  
7  
8  
9  
10  
11  
12  
13  
14  
15  
16  
17  
18  
19  
20  
21  
22  
23  
24  
25  
26  
27  
28  
29  
30  
31  
32  
33  
34  
35  
36  
37  
38  
39  
40  
41  
42  
43  
44  
45  
46  
47  
48  
49  
50  
51  
52  
53  
54  
55  
56  
57  
58  
59  
60  
61  
62  
63  
64  
65

[45] V. A. Saveleva, L. Wang, W. Luo, S. Zafeiratos, C. Ulhaq-Bouillet, A. S. Gago, K. A. Friedrich, E. R. Savinova *J. Phys. Chem. Lett.* 7 (2016) 3240–3245

[46] P. Lettenmeier, J. Majchel, L. Wang, V. A. Saveleva, S. Zafeiratos, E. R. Savinova, J.-J. Gallet, F. Bournel, C. Ulhaq-Bouillet, A. S. Gago, K. A. Friedrich, *Chem. Sci.* 9 (2018) 3570-3579

[47] E. Brightman, J. Dodwell, N. van Dijk, G. Hinds, *Electrochem Commun* 52 (2015) 1-4

[48] D. Zhang, K. Zeng, *Ind. Eng. Chem. Res.* 51 (2012) 13825-13832.

[49] S. Giddey, F.T. Ciacchi, S.P.S. Badwal, *J. Membr. Sci.* 346 (1) (2010) 227-232.

[50] P. Trinke, B. Bensmann, R. Hanke-Rauschenbach, *Electrochemistry Communications* 82 (2017) 98-102

[51] N. Briguglio, S. Siracusano, G. Bonura, D. Sebastián, A. S. Aricò, *Applied Catalysis B: Environmental* 246 (2019) 254-265

[52] S. Siracusano, S. Trocino, N. Briguglio, V. Baglio A. S. Aricò, *Materials* 11 (2018) 1368 - 1383

[53] P. Aßmann, A. S. Gago, P. Gazdzicki, K. A. Friedrich, M. Wark, *Current Opinion in Electrochemistry* 21 (2020) 225-233

[54] B. Verdin, F. Fouda-Onana, S. Germe, G. Serre, P.A. Jacques, P. Millet, *Int J Hydrogen Energy* 42 (2017) 25848-25859

**Table 1.** Survey of main results from ex-situ physicochemical analysis

	Membrane thickness	Bulk elemental analysis of Ir and Ru metals in the anode layer SEM-EDX		Surface elemental analysis of Ir and Ru metals in the anode layer XPS		B.E. Ir 4f <sub>7/2</sub>	B.E. Ru 3p <sub>3/2</sub>	Mean particle size anode	Mean particle size cathode
Units	μm	Ir at. %	Ru at. %	Ir at. %	Ru at. %	eV	eV	nm	nm
FRESH MEA	90 ± 2	70.1 ± 0.5	29.9 ± 0.5	75.4 ± 2.0	24.6 ± 2.0	62.18	463.48	6 ± 2.0	2.5 ± 0.5
MEA operate in steady-state mode	81 ± 3	70.7 ± 0.5	29.3 ± 0.5	76.2 ± 2.0	23.8 ± 2.0	61.50	462.67	6 ± 2.0	3.0 ± 0.5
MEA operated with load and thermal cycles	84 ± 3	76.7 ± 0.5	23.3 ± 0.5	80.3 ± 2.0	19.7 ± 2.0	61.82	462.84	5 ± 2.0	3.5 ± 0.5

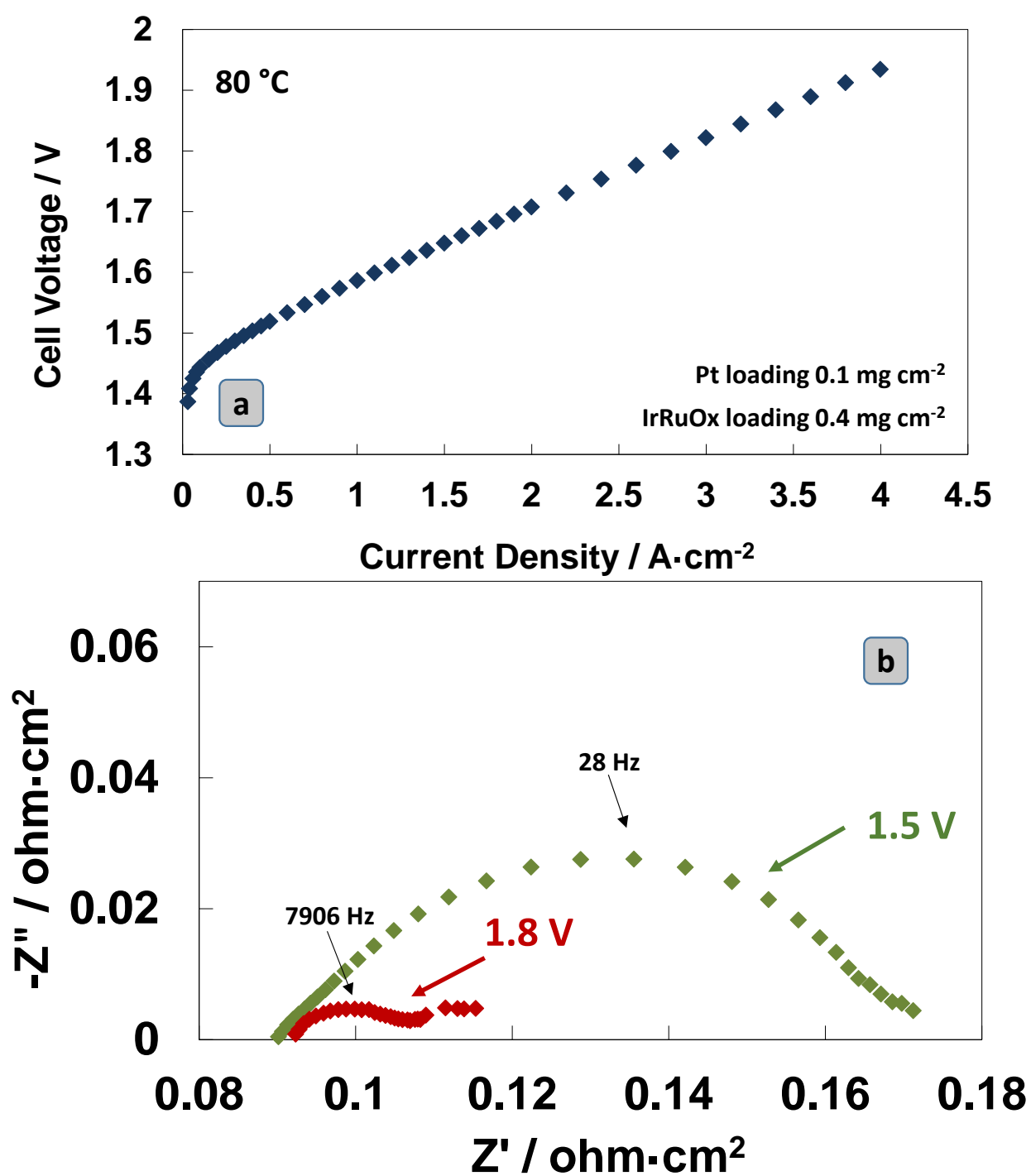


**Fig. 1** (a) Polarization curves at 80 °C and (b) ac-impedance spectra at 1.5 V and 1.8 V for the fresh PEM electrolysis MEA

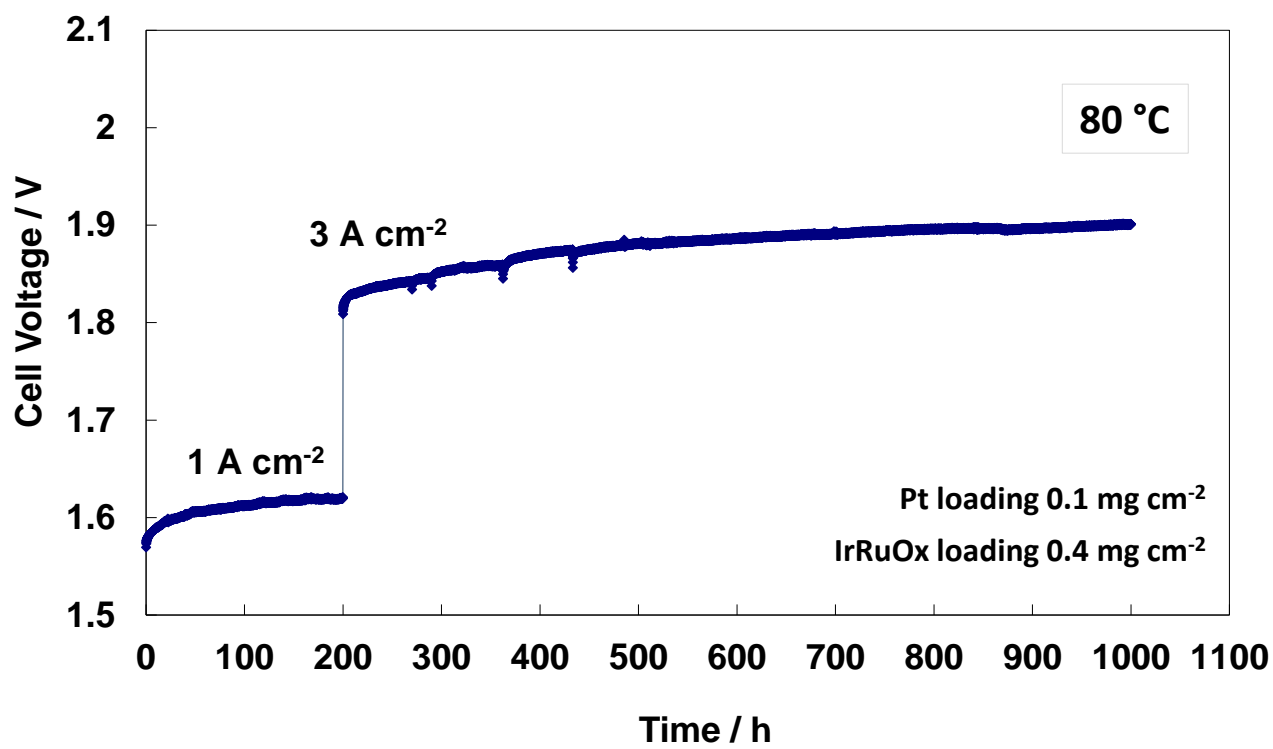


**Fig. 2** MEA steady-state durability test at 1 and 3 A cm<sup>-2</sup> and 80 °C

Figure 3

[Click here to download Figure\(s\) - provided separately: Fig 3.docx](#)

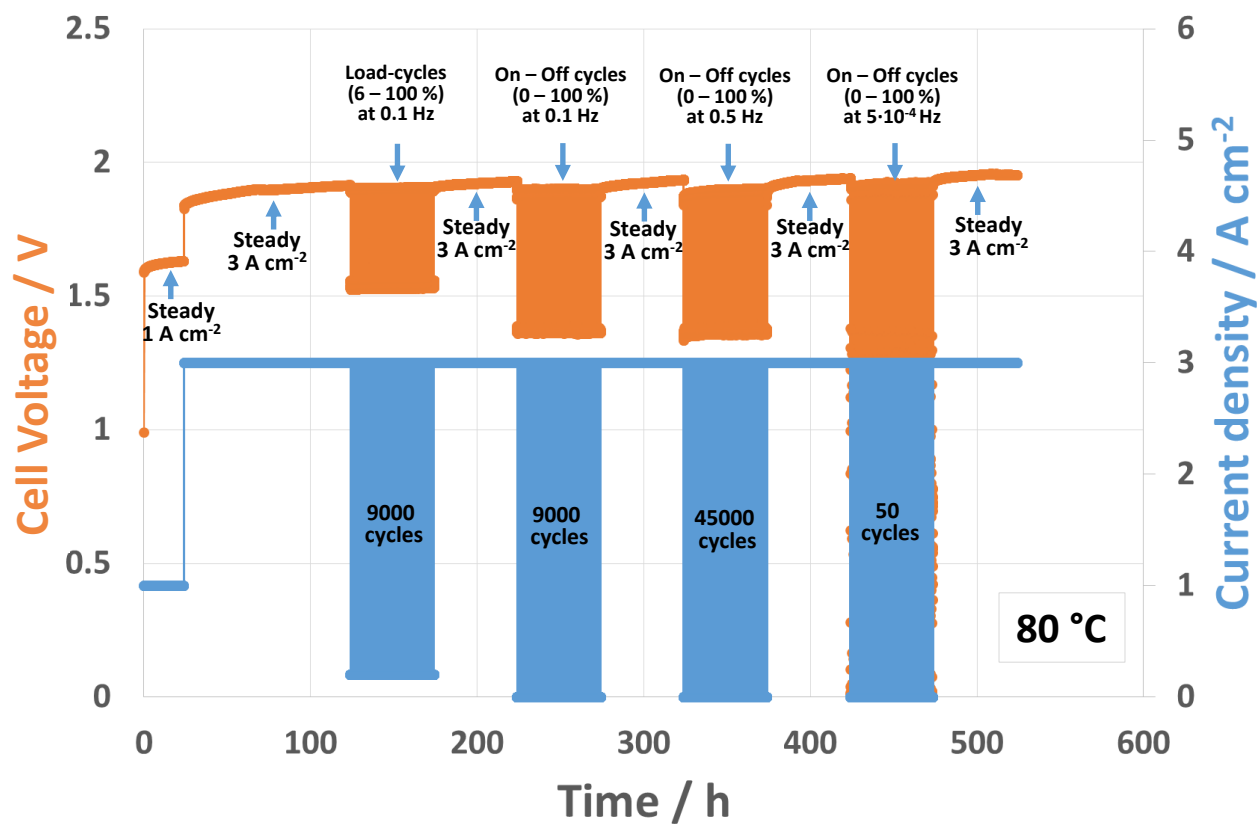


**Fig 3** MEA current density (load) cycles at 80 °C; Pt loading: 0.1 mg·cm<sup>-2</sup>;

IrRuOx loading: 0.4 mg·cm<sup>-2</sup>

Figure4

[Click here to download Figure\(s\) - provided separately: Fig 4revised.docx](#)

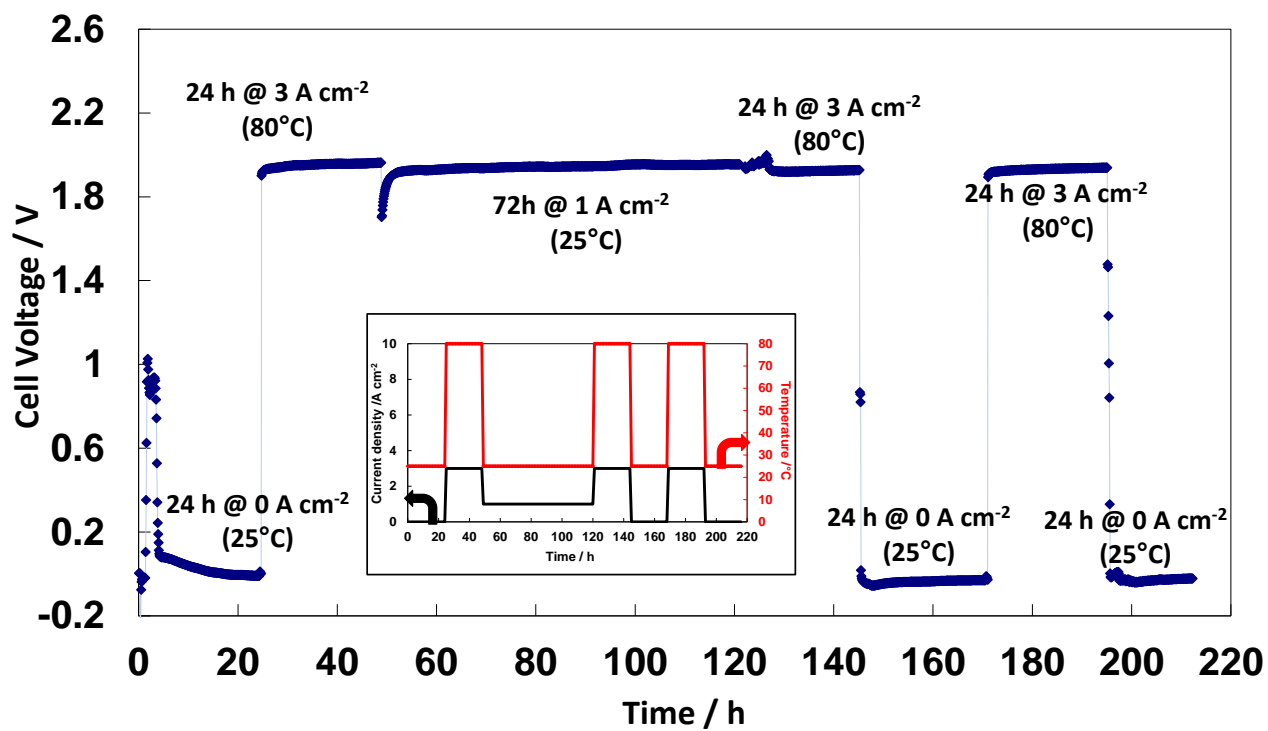
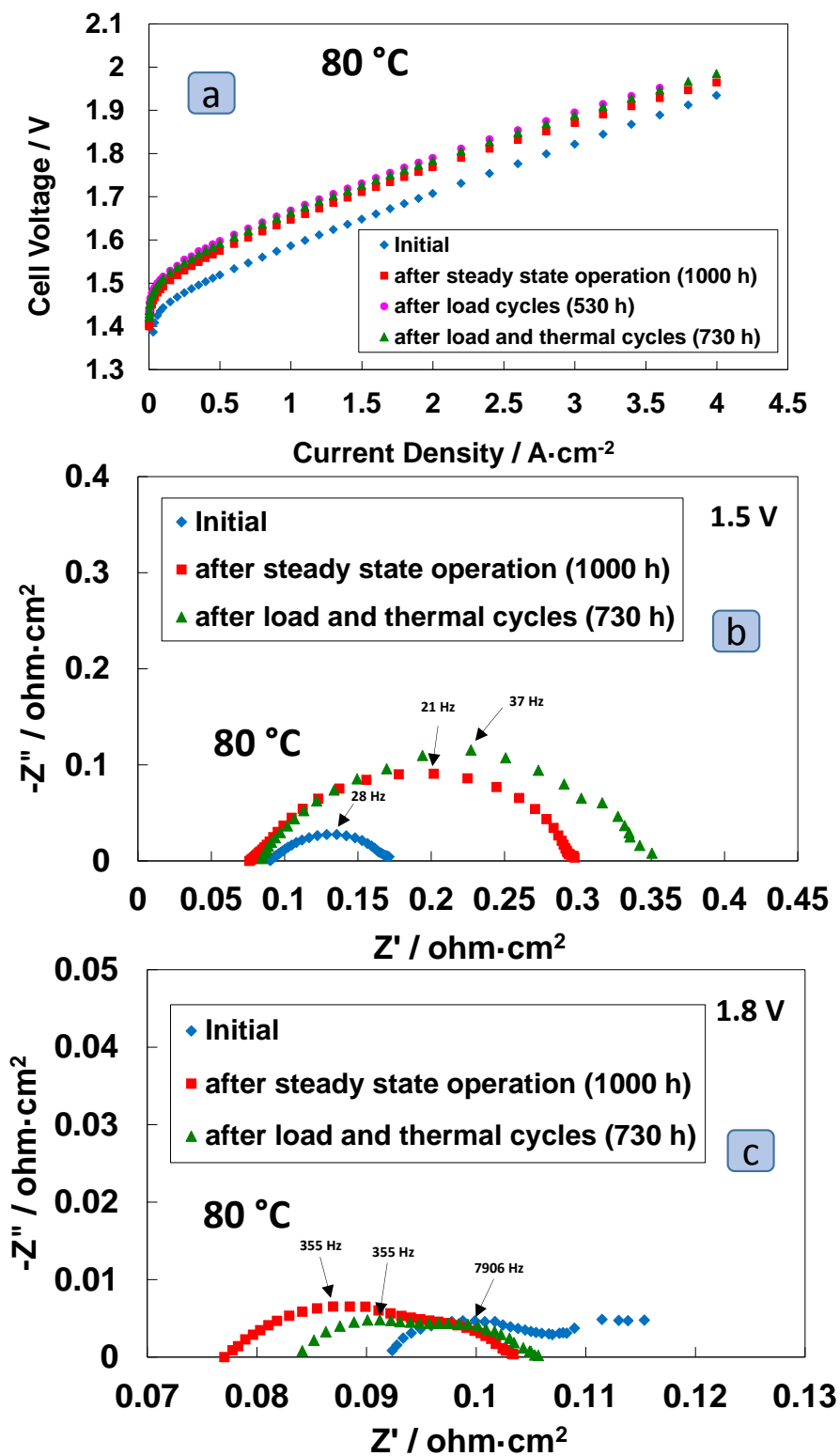


Fig. 4 Temperature and current cycling of the PEM electrolysis MEA; the test protocol is shown in

the inset; Pt loading: 0.1 mg cm<sup>-2</sup>; IrRuOx loading: 0.4 mg cm<sup>-2</sup>

Figure 5

[Click here to download Figure\(s\) - provided separately: Fig 5.docx](#)



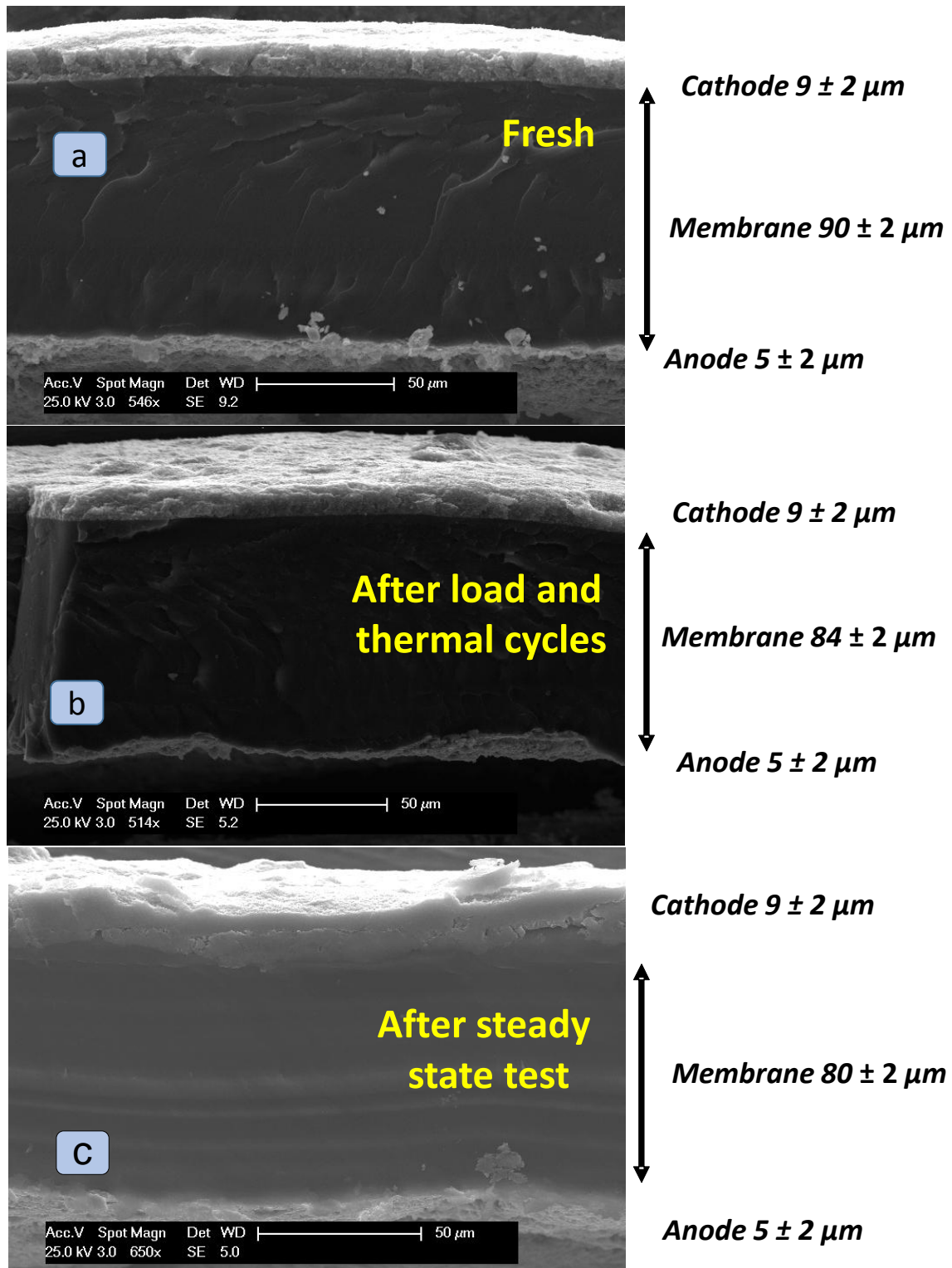
**Fig. 5** MEA polarization curves (a) and impedance spectroscopy at 1.5 V (b) and 1.8 V (c) before and after steady-state durability and cycle tests; Pt loading: 0.1 mg·cm<sup>-2</sup>; IrRuOx loading: 0.4 mg·cm<sup>-2</sup>



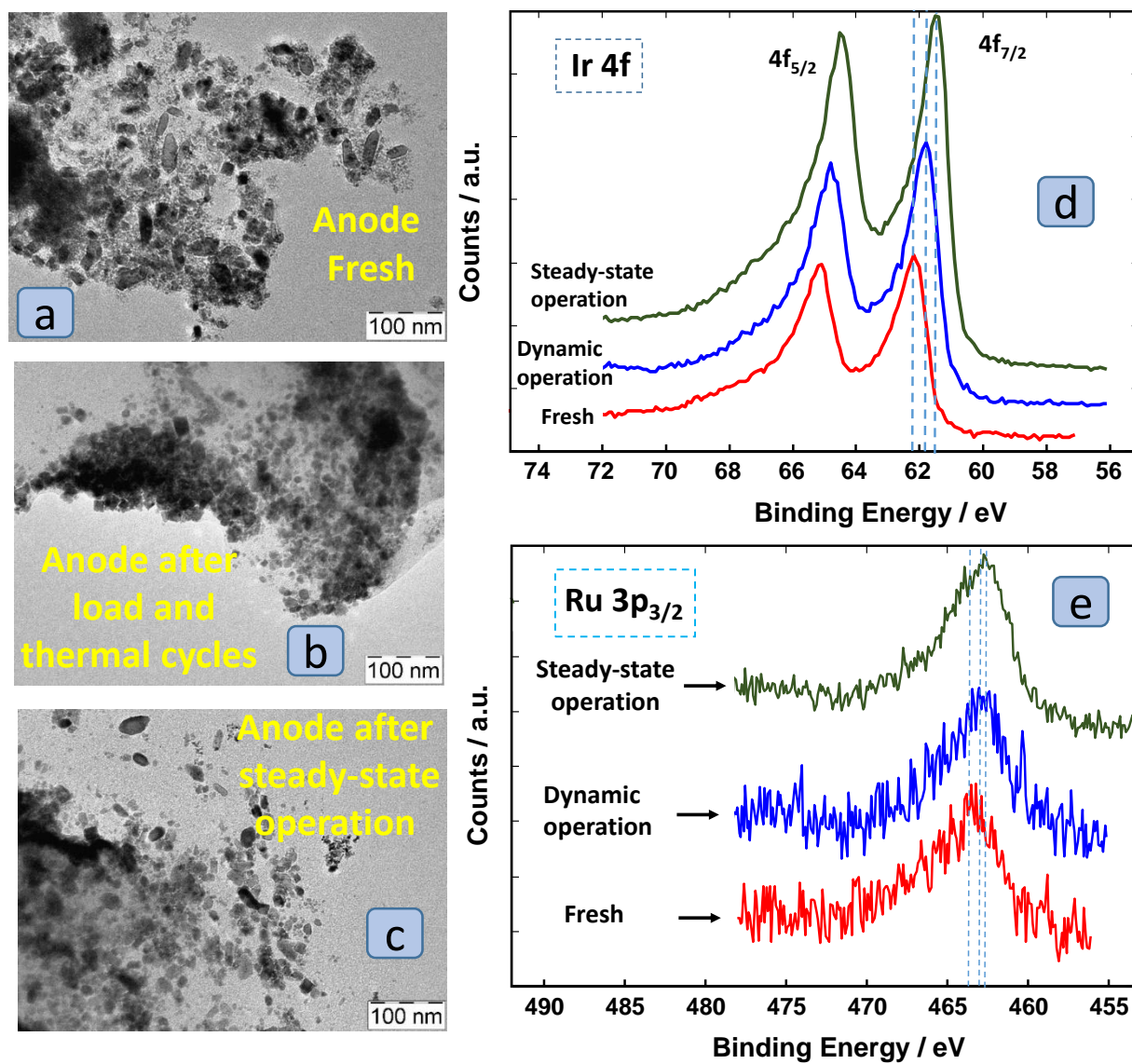


Figure6

[Click here to download Figure\(s\) - provided separately: Fig 6revised.docx](#)



**Fig. 6** SEM Cross-sections of fresh (a) and used MEAs subjected (b) to combined 740 h load and thermal cycles (c) and to 1000 h steady-state electrolysis operation (the cathode layer is shown on the top for all MEAs)



**Fig. 7** TEM images for the fresh anode (a), the anode after 740 h load and thermal cycles (b), and the anode after 1000 h steady-state operation (c); high resolution Ir 4f (d) and Ru  $3p_{3/2}$  (e) XPS analyses before and after the 740 h combined electrolysis cycling tests (dynamic operation) and 1000 h steady-state operation.



## Figure 8

[Click here to download Figure\(s\) - provided separately: Fig 8 revised.docx](#)

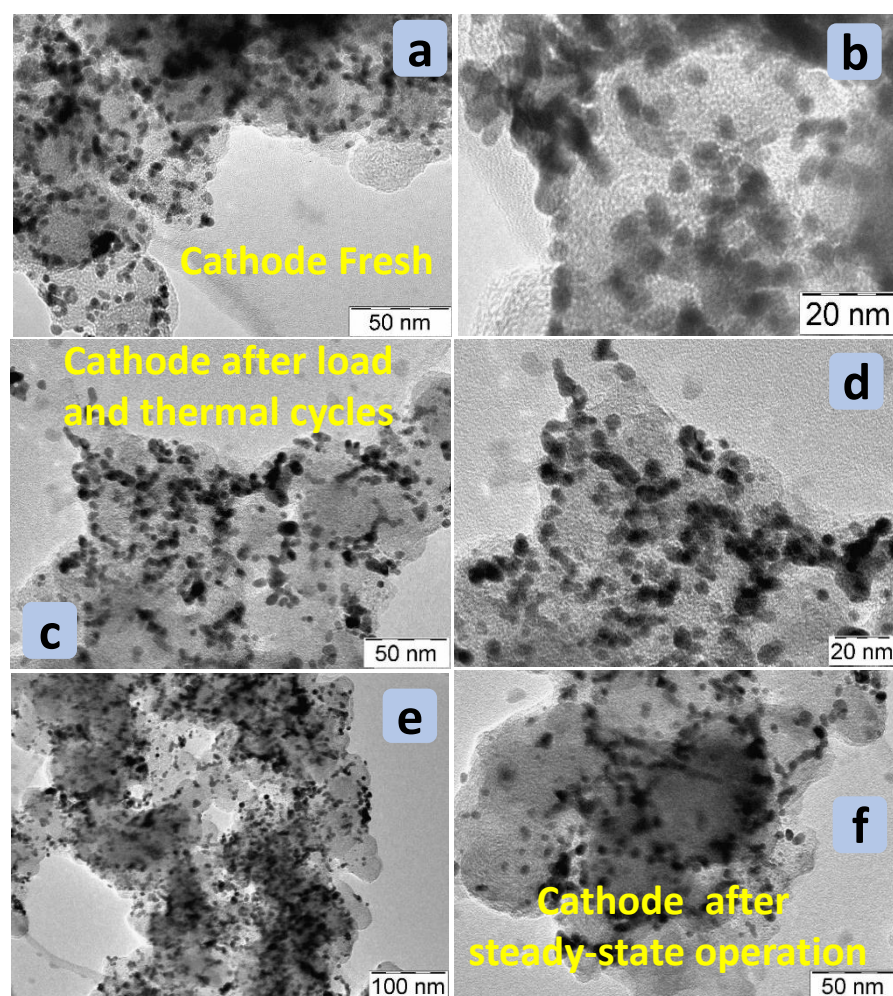


**Fig. 8** TEM images for the fresh MEA cathode (a-b), the MEA cathode after 740 h load and thermal cycles (c-d), and the MEA cathode after 1000 h steady-state durability test (e-f).

**Supplementary Materials**

[Click here to download Supplementary Materials: Supplementary Material revised.docx](#)